MATEMATICKO-FYZIKÁLNÍ FAKULTA
Univerzita Karlova

BAKALÁŘSKÁ PRÁCE

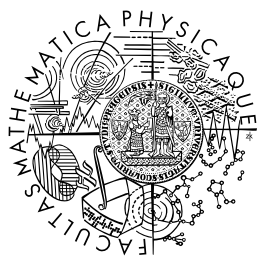Dominik Vach

Anelastická deformace planetárních těles

Katedra geofyziky

Vedoucí bakalářské práce: prof. RNDr. Ondřej Čadek, CSc.

Studijní program: Fyzika

Studijní obor: Obecná fyzika

Praha

FACULTY
OF MATHEMATICS
AND PHYSICS
Charles University

BACHELOR THESIS

Dominik Vach

Anelastic deformation of planetary bodies

Department of Geophysics

Supervisor of the bachelor thesis: prof. RNDr. Ondřej Čadek, CSc.

Study programme: Physics

Study branch: General Physics

Prague 2016

I declare that I carried out this bachelor thesis independently, and only with the cited sources, literature and other professional sources.

I understand that my work relates to the rights and obligations under the Act No. 121/2000 Sb., the Copyright Act, as amended, in particular the fact that the Charles University in Prague has the right to conclude a license agreement on the use of this work as a school work pursuant to Section 60 subsection 1 of the Copyright Act.

In .... date ....

Title: Anelastic deformation of planetary bodies

Author: Dominik Vach

Department: Department of Geophysics

Supervisor: prof. RNDr. Ondřej Čadek, CSc., Department of Geophysics

Abstract: Observations indicate an existence of subsurface oceans for some of the icy moons in the Solar System which are heated by the tidal forces. In order to describe this anelastic deformation, the methods well-known from the continuum mechanics were employed, and thus the dissipation was calculated for various bodies. In the thesis, Maxwell and Kelvin-Voigt model were compared in their ability to predict the heating power of the bodies. In contrast to the Maxwell model, the Kelvin-Voigt model, which is generally not used in geophysics, represents reversible processes, and thus could explain the effects which are otherwise explained only by the gravity. A program in Fortran was developed in order to compare the models by modelling 3D anelastic deformation of planetary bodies under the effect of tidal forces. The results indicate the predicted power can be various for both models and Kelvin-Voigt model could be used e.g. to describe short run deformation processes.

Keywords: tides viscoelasticity dissipation

Název práce: Anelastická deformace planetárních těles

Autor: Dominik Vach

Katedra: Katedra geofyziky

Supervisor: prof. RNDr. Ondřej Čadek, CSc., Katedra geofyziky

Abstrakt: Pozorování naznačují, že některé ledové měsíce ve Sluneční soustavě mají podpovrchové oceány zahřívané působením slapových sil. Pro popis této anelastické deformace je vhodné použít metody známé z mechaniky kontinua a nalézt tak disipovanou energii pro jednotlivá tělesa. V této práci je porovnáván Maxwellův a Kelvin-Voigtův deformační model a jejich schopnost určit tepelný výkon těles. Narozdíl od Maxwellova modelu, obecně nepoužívaný Kelvin-Voigtův model popisuje vratnou deformaci, a tedy by mohl umožňovat popis jevů, které mohou být jinak vysvětleny pouze pomocí gravitačních účinků. Za účelem porovnání obou modelů pro různá tělesa byl vyvinut program ve Fortranu, který modeluje 3D anelastickou deformaci planetárních těles za přítomnosti slapové síly. Výsledky naznačují, že předpovězený výkon může být různý v závislosti na použitém modelu a že Kelvin-Voigtův model by mohl najít uplatnění například v krátkodobých procesech.

Klíčová slova: slapy viscoelasticita disipace

Contents

Introduction

It has been over 26 years since the launch of the unmanned spacecraft Galileo and over 18 years since the launch of the unmanned spacecraft Cassini. Both were named after famous astronomers and discoverers of the largest satellites of the planets the spacecrafts were sent to. In case of Galileo the Jupiter's orbit has been entered, and thus many planetary bodies could have been studied more precisely from the incoming data. Nonetheless, a similar mission to more distant Saturn was scheduled for the Cassini spacecraft eight years later. Since that time, both spacecrafts have discovered a wonderful and exciting world of icy moons such as e.g. Jupiter's moon Europa or Saturn's moon Enceladus. The obtained data suggested that some of these icy moons could have had vast subsurface oceans comprised of liquid water as studied by Tobie et al. (2008). This indication raised a question what was the origin of the energy which could make the heat in the oceans sustainable.

The distance of the Sun, the Solar System's biggest source of energy, is substantial from these satellites and the surface temperatures are very low (on average 102 K in case of Europa and 75 K in case of Enceladus) (Prockter & Pappalardo 2007). The low temperatures point at the fact that there are no or little radiogenic elements contained in the ice mantle whereas in case of terrestrial planetary bodies it is considered to be a main source of energy.

It turns out the source of the heat, which is very important in case of some of the icy moons, is the tidal heating as shown by Chen et al. (2014). Usually the rotation of the satellites gradually slows down until they reach the synchronous rotation with the body they orbit as a result of the effect which is called a tidal braking. Even though Enceladus and Europa have synchronous rotation, they do not have zero eccentricity of their elliptical trajectories which expose them to the stronger deformation effects when they are nearby the planet they orbit and weaker effects when they are further, hence making the tidal force an important player in the source of heat question which was examined in case of Enceladus by Tyler (2009).

However, the deformation of the planetary bodies is neither purely elastic nor purely viscous, and thus there is an urge to use a model containing both of these characteristics. In physics there is a long tradition of implementing the so called Q-factor which measures the relative loss of energy in case of periodically damped processes. That corresponds to the periodically influenced icy moon by the tidal forces quite well, however, this approach does not allow to implement more detailed characteristics about the structure of the planets and rather combine all the characteristics in only one number.

Therefore, the approach has moved towards a more precise description of the energy dissipation using the continuum mechanics. The problem with this method is that it is difficult to measure the exact parameter values for the distant astronomical bodies and the laboratory measurements can be imprecise because the materials could behave differently on very large scales.

Geophysicists traditionally use the so called Maxwell rheology in order to describe the relationship between the material parameters and its deformation. This rheology quickly became very popular in the geophysical community as it

managed to satisfactorily explain the surface movements as a result of the post-glacial rebound on Earth which can be seen e.g. in Peltier et al. (1986). However, despite its massive use, it is valid approximation only in case of long term lasting processes. Further limitation is that according to the Maxwell rheological model the deformation process is irreversible and the model thus relies on the gravitational effects to ensure the possible reversible processes which was studied by Zhong & Zuber (2000).

It raises a question whether the model should be used also in case of the icy moons where the processes might not necessarily be irreversible as they are incomparably smaller than Earth. There are several other deformation models used predominantly in material engineering and some of them are reversible. In this thesis the aim is to compare the irreversible Maxwell model with the reversible Kelvin-Voigt model in order to find out how useful this alternative approach might be in the description of the dissipation as the source of the heat.

In order to do so, the computer program which uses the spectral methods in three dimensions was developed and tested by the author. Consequently, a series of calculations were made for different types of planetary bodies in order to show the effect of their particular attributes on the usefulness of the two compared models.

The structure of the paper is as follows: The first chapter is devoted to the theoretical differences between the Maxwell and Kelvin-Voigt model and there are some formulas derived for their applications in one-dimensional case. The second chapter introduces the partial differential equations which describe the physical intuition behind the three dimensional deformation model and the equations are transformed in the spectral form. The second chapter further shows the numerical discretization of the spectrally decomposed model and its algebraic solution valid for purely elastic model. The elasticity is then replaced by the Maxwell and Kelvin-Voigt model bringing thus the link to the tidal forces and tidal heating. The last chapter comprises of the results followed by their discussion.

1. Anelastic deformation

Some planets and moons within the Solar System have significantly solid structures, and hence they are able to record the history of individual geological events. The bodies which are predominantly fluid such as the gas giants are incomparable in their ability to preserve the history. However, no matter what the structure of the planetary body is, from the long timescale view, the most of planetary bodies behave similarly to fluids (it is only a matter of time), and thus effects such as the flow of mass can be observed there.

As the bodies behave like the fluids, the mass inside may stir both horizontally and vertically. During this stirring process there occurs a friction which can be similarly as in the material engineering described by physical parameters such as viscosity or shear modulus.

Whilst some of the materials, like honey or ketchup, behave in a viscous way and thus do not return back to their initial position when the force acting upon the object subsides, other materials, like rubber, may be almost entirely elastic which means they are completely resistant to any distorting influences or stress and they return to their original shape when the stress is removed.

Nevertheless, the two mentioned approaches (purely elastic or purely viscous extremes) are actually only theoretical and the materials always exhibit both elastic and viscous characteristics as we can see in many applications e.g. in (Tobie et al. 2008). Hence, the planetary bodies behave in the same way, too, and thus it is possible to apply classical viscoelastic deformation models such as Maxwell or Kelvin-Voigt models which is especially done in this thesis.

1.1 Mechanical analogs

Let us introduce the concept of the mechanical analogs which is a simplified scheme used in the material engineering in order to improve the notion of how the viscoelasticity can be understood. The most simple mechanical analogs are composed of only one element. In this thesis, there are only two kinds of elements used, i.e. on the one hand purely elastic elements represented in diagrams by springs, and on the other hand purely viscous elements represented in diagrams by dashpots.

The studied process comprises three stages. The first one occurs when the model is in its initial position without any forces acting upon the analogs. The second stage describes what happens if some force strains the loose end of the model and fixes it in a non-default position. The last stage shows what happens when the fixing is released, and thus demonstrates whether the process is reversible or not. These three stages are depicted in the Fig. 1.1 for both elastic component and viscous component.
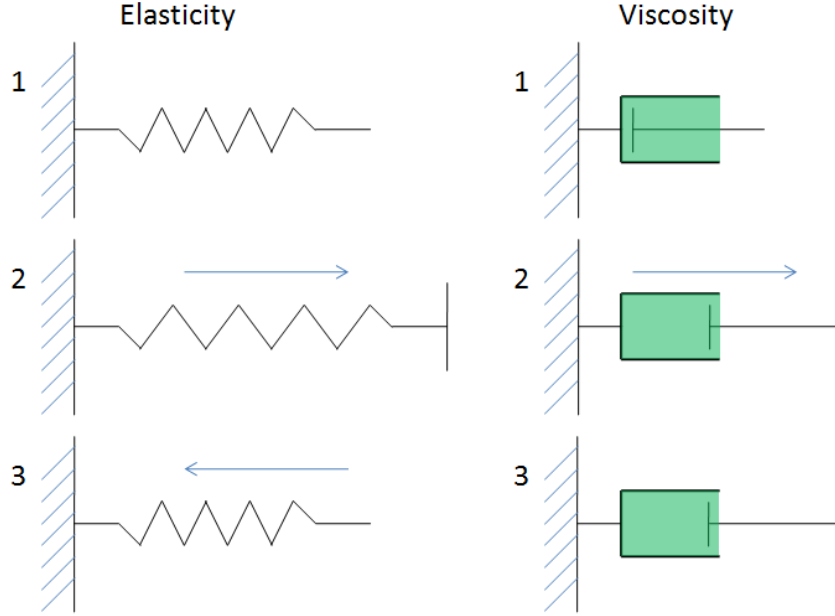
Figure 1.1: Mechanical analogs scheme showing the difference between the elasticity and viscosity in terms of reversibility.

It is noticeable that in contrast to the elastic component, the main difference lies in the irreversibility of the viscous process. This irreversibility is an important concept in terms of dissipation and hence provides the link to the leak of energy out of the system. However, as the realistic materials are neither purely elastic nor purely viscous, the solution consists of combination of both as it is done e.g. in Maxwell and Kelvin-Voigt model.

Interestingly, all these viscoelastic models are made up from the elastic and viscous component by connecting them equivalently as it is done in case of electrical circuits and thus creating an infinite number of possibilities how to connect them (either in series or in parallel). In this thesis we focused on the two simplest models each constituted by both elastic and viscous parts composed only of two components once connected in series, for the second time in parallel.

In spite of the existence of a plenty of more complicated models such as SLS (Standard Linear Solid) model or Generalized Maxwell model also known as the Maxwell-Wiechert model, the purpose of this thesis is not to find the model which suits the best but rather to show how other approach can lead to different results and thus question the currently established using of Maxwell model used e.g. by Ross & Schubert (1989) or Tobie et al. (2008). From this reason, only the Maxwell model and the Kelvin-Voigt model are examined.

1.2 Maxwell model

Maxwell model consists of a spring and a dashpot connected in series, and therefore represents a combination of a reversible and an irreversible process. In terms of mechanical analogs the whole model can be summarized by Fig. 1.2, which is divided into three stages which are exactly the same as was discussed in the sec-

tion 1.1 except for the fact that stage 2 is subdivided between the part 2a which stands for an immediate change as the whole material is pulled on and fixed afterward and the part 2b which refers to what would happen if the material was fixed in such a position for a very long time.
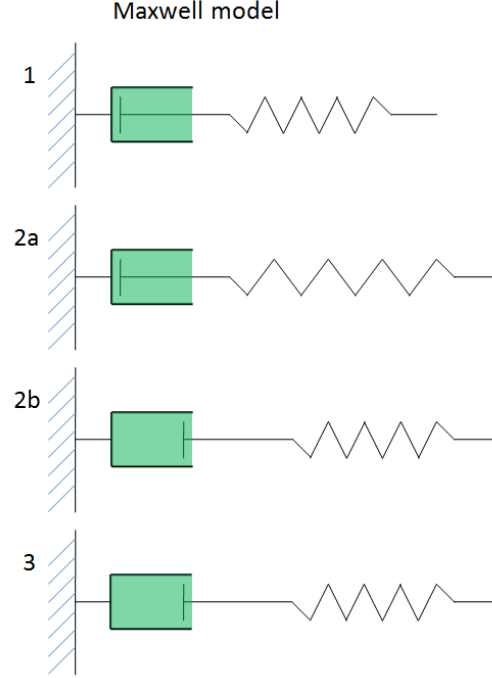
Maxwell model

Figure 1.2: Mechanical analogs scheme showing the irreversibility in case of the Maxwell model.

The pulling of the material is followed by an immediate reaction of the spring whereas the dashpot stays at its initial position because it resists the force. However, all the energy stored in the spring will gradually transfer towards the dashpot resulting in the stage 2b. Finally, if the fixing is removed, the dashpot is unable to return to its initial position, and thus the Maxwell model represents the irreversible process which is caused by the occurrence of the dissipation on the dashpot. Let us take a closer look at the whole model more mathematically.

The key aspect of the Maxwell model is the assumption that the stress σ measurable on both components is equal to each other. (Roylance 2001) In contrast to this property, the strain on the separate components sums up to the total strain ε. Formally these two observations can be written as

$$\sigma = \sigma_E = \sigma_V, \tag{1.1}$$

$$\varepsilon = \varepsilon_E + \varepsilon_V, \tag{1.2}$$

where the subscript $_E$ stands for the variables referring to the elastic part of the model (spring) and the subscript $_V$ stands for the variables referring to the viscous part of the model (dashpot).

From the Hooke's law it follows that there exists a relation between the stress and the strain measured individually on each of the components of the model.

The relation for the elastic parts (springs) can be summarized by the following equation

$$\sigma_E = 2\mu\varepsilon_E, \tag{1.3}$$

where μ is the shear modulus. It can be noticed that the stress produced on the elastic component is proportionally dependent on the strain which is usually in case of only elastic component occuring caused by acting of a force.

Similarly, there exists also a variant of Hooke's law for the viscous component and is described by the following equation

$$\sigma_V = 2\eta\dot{\varepsilon}_V, \tag{1.4}$$

where η is the viscosity and the dot symbol stands for the time derivative.

If we take a time derivative of Eq.(1.2), we obtain

$$\dot{\varepsilon} = \dot{\varepsilon}_V + \dot{\varepsilon}_E. \tag{1.5}$$

If Eqs.(1.3) and (1.4) are substituted into Eq.(1.5), taking into consideration that the stress is the same on all components (from Eq.(1.1)), we obtain the following differential equation

$$\dot{\varepsilon} = \frac{\sigma}{2\eta} + \frac{\dot{\sigma}}{2\mu}. \tag{1.6}$$

From the model represented by mechanical analogs, it is obvious that the strain ε is held constant in the stage 2a and 2b, which gives us formally the following condition

$$\dot{\varepsilon} = 0. \tag{1.7}$$

If the condition is substituted into Eq.(1.6), a solvable differential equation is obtained

$$0 = \frac{\sigma}{2\eta} + \frac{\dot{\sigma}}{2\mu}, \tag{1.8}$$

with a general solution

$$\sigma(t) = \sigma_0 \exp\left(-\frac{t}{\tau}\right), \tag{1.9}$$

where σ_0 is the constant denoting the initial stress, τ is the fraction of viscosity over shear modulus $(\tau = \frac{\eta}{\mu})$ sometimes denoted as relaxation time and t is the time.

This equation describes an exponential decrease in the stress acting upon both components in the Maxwell model. As the time elapsed since the fixing of the material increases $(t \rightarrow \infty)$, the stress approaches so called hydrostatic limit, where the stress on the both components fades away.

1.3   Kelvin-Voigt model

The Kelvin-Voigt model is made out of a spring and a dashpot too, but this time they are connected in parallel. The most significant difference between the two models is that the Kelvin-Voigt model is a reversible process, as the energy which is dissipated by the dashpot cannot slip out of the model completely due to its connection to the spring which will return the dashpot to its initial position. The

situation with the mechanical analogs is depicted in the Fig.1.3 exactly in the same way as was in the section 1.1.
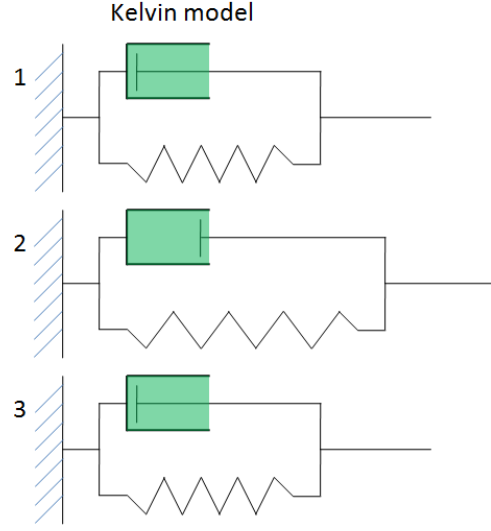

Figure 1.3: Mechanical analogs scheme showing the reversibility in case of the Kelvin-Voigt model.

It can be seen that as we keep the force acting upon the material constant, both dashpot and spring pulls on (stage 2). When this force disappears, the material returns gradually to its initial position (stage 3) where no force acts upon the material. This time the model is not fixed as in the case of Maxwell model, the model is only pulled on by a constant force, which results in a constant stress. The mathematical model behind is thus quite different to the Maxwell model.

In Kelvin-Voigt model, both components must have exactly the same strain ε whereas the stress acting upon the components will sum up to the total stress σ. This means the key equations are formed exactly vice versa in comparison to the equations introduced for Maxwell model. (Roylance 2001) Formally it can be rewritten as

$$\sigma = \sigma_E + \sigma_V, \tag{1.10}$$

$$\varepsilon = \varepsilon_E = \varepsilon_V, \tag{1.11}$$

where the notation is the same as in the case of Maxwell model.

The equations for the relations between the stress and the strain derived in the section of the Maxwell model (i.e. Eqs.(1.3) and (1.4)) continue to hold. Analogously to the previous model, let us take a first derivative with respect to time from the equation (1.10).

$$\dot{\sigma} = \dot{\sigma}_V + \dot{\sigma}_E. \tag{1.12}$$

If Eqs.(1.3) and (1.4) (relations between the stress and the strain) are substituted into Eq.(1.10), taking into consideration that the strain the same is on all components (from Eq.(1.11)), the following differential equation is obtained

$$\sigma = 2\eta\dot{\varepsilon} + 2\mu\varepsilon. \tag{1.13}$$

If we take a time derivative of Eq.1.13 we obtain

$$\dot{\sigma} = 2\eta\ddot{\varepsilon} + 2\mu\dot{\varepsilon}. \tag{1.14}$$

As has been noted previously and also from the model represented by mechanical analogs, we assume the force (and therefore stress) to have a constant value during the pulling (stage 2), which gives us the following condition on the stress

$$\dot{\sigma} = 0. \tag{1.15}$$

If the condition is substituted into Eq.(1.14), a solvable differential equation of order two is obtained

$$0 = 2\eta\ddot{\varepsilon} + 2\mu\dot{\varepsilon}, \tag{1.16}$$

with a general solution assuming no initial strain $(\varepsilon(0) = 0)$

$$\varepsilon(t) = \varepsilon_0 \left[1 - \exp\left(-\frac{t}{\tau}\right)\right], \tag{1.17}$$

where ε_0 is the constant denoting the strain which would occur if the model was elastic, τ is similarly as in the Maxwell model the fraction of viscosity over shear modulus $(\tau = \frac{\eta}{\mu})$ sometimes denoted as relaxation time and t is the time.

This equation shows us how the material gradually relaxes over the time when the force is present. As the time elapsed increases $(t \to \infty)$, the strain ε approaches so called elastic limit, where the strain on both components is equal to the fixed value of ε_0.

1.4 Dissipation

In the previous section, the Kelvin-Voigt model has been thoroughly examined. Let us now take a closer look on the dissipative process which proceeds on the viscous part.

The most simple model of an elastic Hookean spring can be put into motion by adding a weight m on the spring of stiffness k. This causes an infinitely lasting oscillating movement described by the equation of motion

$$m\ddot{x} = -kx, \tag{1.18}$$

where x is the deviation of the spring. Consequently, this oscillating process can be slowed by a friction or a damping process. In the viscoelastic models, the component responsible for the damping is the viscous part represented by the dashpot. As this damping process acts against the movement of the weight, the damping term is added to Eq.(1.18) creating thus

$$m\ddot{x} = -kx - c\dot{x}, \tag{1.19}$$

where c is the viscous damping coefficient. This differential equation can be rewritten in the form

$$\ddot{x} + 2\zeta\omega\dot{x} + \omega^2 x = 0, \tag{1.20}$$

where $\omega = \sqrt{\frac{k}{m}}$ is called the undamped angular frequency of the oscillator, $\zeta = \frac{c}{2\sqrt{mk}}$ is the damping ratio. If $\zeta > 1$ the oscillator is then overdamped which means

it exponentially decays to steady state and is not oscillating at all. If $\zeta < 1$ the oscillator is said to be underdamped which makes it oscillate with decreasing amplitude to zero. Last but not least, if $\zeta = 1$ the oscillator is critically damped which means it returns to the steady state as quickly as possible and does not perform any oscillations.

If a weight is added on the Kelvin-Voigt material instead of a Hookean spring, and thus causing the stress on both components, the material will start to oscillate as a consequence with damping via the dashpot. The equation (1.10) for the total stress in the material is stated in the previous section, and can be used in this moment to analyze the dissipation. Let us rewrite the total stress according the equation of motion

$$\sigma = \frac{F}{A} = \frac{m\ddot{\varepsilon}}{A} = \rho_A \ddot{\varepsilon}, \qquad (1.21)$$

where F is the force, A is the area where the force is acting and ρ_A is the area density defined as $\rho_A = \frac{m}{A}$. If we substitute the Eqs.(1.3) and (1.4) in the Eq.(1.10) using the Eq.(1.21), we obtain

$$\rho_A \ddot{\varepsilon} + 2\mu\varepsilon + 2\eta\dot{\varepsilon} = 0, \qquad (1.22)$$

which can be consequently rewritten as

$$\ddot{\varepsilon} + \frac{2\eta\dot{\varepsilon}}{\rho_A} + \frac{2\mu\varepsilon}{\rho_A} = 0, \qquad (1.23)$$

and finally transformed to the similar shape as in Eq.(1.20)

$$\ddot{\varepsilon} + 2\zeta\omega\dot{\varepsilon} + \omega^2\varepsilon = 0, \qquad (1.24)$$

where $\omega = \sqrt{\frac{2\mu}{\rho_A}}$ and $\zeta = \eta\sqrt{\frac{2}{\mu\rho_A}}$ this time. The amount of the dissipation can be measured by the so called Q factor, which is defined as

$$Q = 2\pi \times \frac{E}{\Delta E}, \qquad (1.25)$$

where E is the total stored energy in the oscillator and ΔE is the energy lost per one period of oscillation. In this case the Q factor can be computed from the damping ratio according to formula

$$Q = \frac{1}{2\zeta}. \qquad (1.26)$$

The total energy E stored in the model over time t can be computed via the following equation which is analogous to the one specified in Tobie et al. (2008)

$$E = \int_0^{\varepsilon_{max}} \sigma d\varepsilon = \int_0^t \sigma\dot{\varepsilon}dt', \qquad (1.27)$$

where ε_{max} is the maximal strain during the dissipation process.

In the thesis we deal with two viscoelastic models, which modifies the preceding equation to (in case of the time is an oscillation period T which eliminates the elastic part)

$$E_{dis}^{Maxwell} = \int_0^T \sigma\dot{\varepsilon}_V dt', \qquad (1.28)$$

10

in case of the Maxwell model and

$$E_{dis}^{Kelvin} = \int_0^T \sigma_V \dot{\varepsilon} dt', \qquad (1.29)$$

in case of the Kelvin-Voigt model. The intuition behind is that the dissipation proceeds only on the viscous part and therefore the integral for the elastic component is in both cases equal to zero.

2. Mathematical model

In the thesis, the aim is to compare the two separate deformation models as it was described in the previous chapter. This time, however, the application is, at least for one of them, different than usual. Even though it is quite common to use both Maxwell and Kelvin models (or more complex ones) in the material engineering, the planetary deformation research is using predominantly Maxwell model.

In order to numerically test these models and also due to the spherical symmetry of the most of planetary bodies (theoretical), the spectral method was chosen as it effectively decomposes radial and toroidal properties of the bodies. The goal of this chapter is both to describe how the spectral decomposition can be made specifically for these two models and also how to test the two studied models numerically against each other.

2.1 Governing equations

The most important for the numerical simulations of any physical model is its mathematical counterpart described by equations which should be as general as possible. For these reasons the following system of three partial differential equations outlining the physical relationships between the pressure (more precisely the stress tensor) and the displacement of the mass is utilized and we thus follow Tobie et al. (2008) in their numerical setup.

$$\nabla \cdot \vec{u} = 0, \tag{2.1}$$

$$\mathbf{D} = \mu((\nabla \vec{u}) + (\nabla \vec{u})^T), \tag{2.2}$$

$$\nabla \cdot \boldsymbol{\tau} + \vec{f} = 0, \tag{2.3}$$

where $\vec{u}$ is the displacement, $\mathbf{D}$ is the deviatoric part of the Cauchy stress tensor $\boldsymbol{\tau}$, μ is the shear modulus and $\vec{f}$ is some external force.

The equation (2.1) stands for continuity equation, which describes the transport of the mass and it intuitively means that the mass displacement cannot emerge or disappear, there must always be balance between the mass that enters in the chosen point and the mass that exits from it. The equation (2.2) gives us a rheological relationship and is useful as it creates a link between the displacement of the mass and the Cauchy stress tensor based on the material parameters of the mass. The rheological relationship holds for purely elastic models in order to make it more simple. Later, this relationship will be changed to anelastic Maxwell or Kelvin-Voigt model. Last but not least, the equation (2.3) represents the equation of motion, which explains the dynamics of the mass when it is exposed to some exogenous force.

The intuition behind the model that will be constructed consequently is that it should describe a spherical shell of any planetary body with a specified material parameters ρ and μ. It is thus composed not only of these three partial differential equations but also of a boundary condition. It sets up a restriction on the traction

vector which is actually the radial component of the Cauchy stress tensor. This restriction controls for unknown parameters outside the spherical shell and helps thus make a proper discretization. We define this condition on the traction vector both at the top and the bottom of the shell according to the same definition

$$\boldsymbol{\tau} \cdot \vec{e}_r + \rho g u_r \vec{e}_r = \vec{T}, \tag{2.4}$$

where $\boldsymbol{\tau}$ is the Cauchy stress tensor, $\vec{e_r}$ is the radial unit vector, g is the gravitational acceleration, u_r is the radial displacement, ρ is the density of the mantle in case of top boundary condition and difference in densities of core and mantle in case of bottom boundary condition and $\vec{T}$ is the force at the surface perpendicular to the mantle. The force is in both cases oriented outside the spherical shell.

2.2 Spectral decomposition

2.2.1 Continuity equation

We apply spectral method on the equation (2.1)

$$\vec{u} = \sum_{j=0}^{\infty} \sum_{m=-j}^{j} \sum_{l=|j-1|}^{j+1} u_{jm}^l(r) \vec{Y}_{jm}^l(\theta, \varphi), \tag{2.5}$$

which can be for $j \geq 1$ rewritten in the following form

$$\vec{u} = \sum_{j=0}^{\infty} \sum_{m=-j}^{j} [u_{jm}^{j-1} \vec{Y}_{jm}^{j-1} + u_{jm}^j \vec{Y}_{jm}^j + u_{jm}^{j+1} \vec{Y}_{jm}^{j+1}]. \tag{2.6}$$

Substituting for $\vec{u}$ into Eq.(2.1) gives us:

$$\sum_{j=0}^{\infty} \sum_{m=-j}^{j} \sum_{l=|j-1|}^{j+1} \nabla \cdot (u_{jm}^l(r) Y_{jm}^{\vec{l}}) = 0, \tag{2.7}$$

which is equivalent e.g. according to Matas (1995) to

$$\sum_{j=0}^{\infty} \sum_{m=-j}^{j} \sum_{l=|j-1|}^{j+1} \left[\sqrt{\frac{j}{2j+1}} \left(\frac{\mathrm{d}}{\mathrm{dr}} - \frac{j-1}{r} \right) u_{jm}^{j-1} - \sqrt{\frac{j+1}{2j+1}} \left(\frac{\mathrm{d}}{\mathrm{dr}} - \frac{j+2}{r} \right) u_{jm}^{j+1} \right] Y_{jm} = 0, \tag{2.8}$$

The useful property of the spectral decomposition lies in the fact that the previous equation can be separated into many equations that are mutually independent as for every combination of j and m the factor in the parenthesis must be equal to zero. The former equation thus can be separated with respect to Y_{jm}, and therefore the following equation is obtained for every j and m

$$\sqrt{\frac{j}{2j+1}} \left[\frac{\mathrm{d} u_{jm}^{j-1}}{\mathrm{dr}} - (j-1) \frac{u_{jm}^{j-1}}{r} \right] - \sqrt{\frac{j+1}{2j+1}} \left[\frac{\mathrm{d} u_{jm}^{j+1}}{\mathrm{dr}} - (j+2) \frac{u_{jm}^{j+1}}{r} \right] = 0. \tag{2.9}$$

After the multiplication by factor $\sqrt{2j+1}$ the equation can be rewritten in the following form

$$A_1 \frac{\mathrm{d} u_{jm}^{j-1}}{\mathrm{dr}} + A_2 \frac{u^{j-1}}{r} + A_3 \frac{\mathrm{d} u^{j+1}}{\mathrm{dr}} + A_4 \frac{u^{j+1}}{r}, \tag{2.10}$$

where $A_1 = \sqrt{j}$, $A_2 = -\sqrt{j}(j-1)$, $A_3 = -\sqrt{j+1}$, $A_4 = -\sqrt{j+1}(j+2)$.

2.2.2 Rheological equation

In this subsection, the spectral form of Eq.(2.2) is derived slightly similarly to the spectral decomposition of the continuity equation except for the first part.

The first step is to present the fact that every tensor of rank 2 can be decomposed into the following three parts, namely the isotropic part which is equivalent to a tensor of rank 0, the antisymmetric part which is a tensor of rank 1 and the traceless symmetric part, which is of rank 2. Any tensor $\boldsymbol{T}$ of rank 2 can thus be formally decomposed into the three parts

$$\boldsymbol{T} = \frac{1}{3}tr(\boldsymbol{T})\boldsymbol{I} + \frac{\boldsymbol{T} - \boldsymbol{T}^T}{2} + \frac{\boldsymbol{T} - \boldsymbol{T}^T + \frac{2}{3}tr(\boldsymbol{T})\boldsymbol{I}}{2}, \qquad (2.11)$$

where $tr(\boldsymbol{T})$ stands for the trace of the matrix $\boldsymbol{T}$, ^{T} is the transposition of a matrix and $\boldsymbol{I}$ is the identity matrix. Let us rewrite the terms in the previous equation as $(T)_0, (T)_1, (T)_2$, respectively, where the subscripts denote the rank of the tensor as it was stated above. If we apply the same logic on $\nabla \vec{u}$, we get the following equation

$$\nabla \vec{u} = (\nabla \vec{u})_0 + (\nabla \vec{u})_1 + (\nabla \vec{u})_2. \qquad (2.12)$$

The second step is to decompose the variables used in the rheological relationship (2.2), i.e. $\mathbf{D}$ and $\nabla \vec{u}$ into spectral forms. The decomposition of the tensor into isotropic, antisymmetric and symmetric traceless components has a very useful property in this context, i.e. the spectral decomposition also separates the used tensor on three parts exactly according to the rank of the resulting tensor with the second superscript representing the rank. Formally, it can be written as

$$\nabla \vec{u} = \sum_{j=0}^{\infty} \sum_{m=-j}^{j} \left[(\nabla \vec{u})_{jm}^{j0} \mathbf{Y}_{jm}^{j0} + \sum_{l=j-1}^{j+1} (\nabla \vec{u})_{jm}^{l1} \mathbf{Y}_{jm}^{l1} + \sum_{l=j-2}^{j+2} (\nabla \vec{u})_{jm}^{l2} \mathbf{Y}_{jm}^{l2} \right], \quad (2.13)$$

$$(\nabla \vec{u})^T = \sum_{j=0}^{\infty} \sum_{m=-j}^{j} \left[(\nabla \vec{u})_{jm}^{j0} \mathbf{Y}_{jm}^{j0} + \left(\sum_{l=j-1}^{j+1} (\nabla \vec{u})_{jm}^{l1} \mathbf{Y}_{jm}^{l1} \right)^T + \sum_{l=j-2}^{j+2} (\nabla \vec{u})_{jm}^{l2} \mathbf{Y}_{jm}^{l2} \right],$$
$$(2.14)$$

$$\mathbf{D} = \sum_{j=0}^{\infty} \sum_{m=-j}^{j} \sum_{l=|j-1|}^{j+1} D_{jm}^{l2}(r) \mathbf{Y}_{jm}^{l2}(\theta, \varphi). \qquad (2.15)$$

The isotropic part of the previous tensors $\nabla \vec{u}$ and $(\nabla \vec{u})^T$ has to be in both cases equal to zero, because the diagonal elements of the matrix $\nabla \vec{u}$ can be expressed as $(\nabla \cdot \vec{u})\mathbf{I}$, which equals to zero because of the Eq.(2.1). The antisymmetrical parts in $\nabla \vec{u}$ and $(\nabla \vec{u})^T$ eliminate each other as it can be seen from its functional form in Eq.(2.11). Therefore, there remains only a symmetric traceless part left in both $\nabla \vec{u}$ and $(\nabla \vec{u})^T$, which can be rewritten as

$$\nabla \vec{u} + (\nabla \vec{u})^T = 2(\nabla \vec{u})_2. \qquad (2.16)$$

If the equation (2.16) is substituted into the rheological relationship (2.2) and consequently decomposed into the spectral form, then e.g. according to Matas

(1995) the following equation holds

$$\mathbf{D} = \sum_{j=0}^{\infty} \sum_{m=-j}^{j} \sum_{l=|j-2|}^{j+2} D_{jm}^{l2}(r)\mathbf{Y}_{jm}^{l2} =$$

$$= 2\mu \sum_{j=0}^{\infty} \sum_{m=-j}^{j}$$

$$\sqrt{\frac{j-1}{2j-1}} \left(\frac{\mathrm{d}}{\mathrm{d}r} + \frac{j}{r}\right) u_{jm}^{j-1}\mathbf{Y}_{jm}^{j-2,2}$$

$$-\sqrt{\frac{(j+1)(2j+3)}{6(2j-1)(2j+1)}} \left(\frac{\mathrm{d}}{\mathrm{d}r} - \frac{j-1}{r}\right) u_{jm}^{j-1}\mathbf{Y}_{jm}^{j,2}$$

$$+\sqrt{\frac{j-1}{2(2j-1)}} \left(\frac{\mathrm{d}}{\mathrm{d}r} + \frac{j+1}{r}\right) u_{jm}^{j}\mathbf{Y}_{jm}^{j-1,2}$$

$$-\sqrt{\frac{j+2}{2(2j+1)}} \left(\frac{\mathrm{d}}{\mathrm{d}r} - \frac{j}{r}\right) u_{jm}^{j}\mathbf{Y}_{jm}^{j+1,2}$$

$$+\sqrt{\frac{j(2j-1)}{6(2j+1)(2j+3)}} \left(\frac{\mathrm{d}}{\mathrm{d}r} + \frac{j+2}{r}\right) u_{jm}^{j+1}\mathbf{Y}_{jm}^{j,2}$$

$$-\sqrt{\frac{j+2}{2j+3}} \left(\frac{\mathrm{d}}{\mathrm{d}r} - \frac{j+1}{r}\right) u_{jm}^{j+1}Y_{jm}^{j+2,2}. \tag{2.17}$$

By comparing the right hand side of the equation with the left hand side and separating it according to particular spectral parameters j and m, the following five equations can be obtained $\forall j, m$

$$\tau_{jm}^{j-2,2} = 2\mu\sqrt{\frac{j-1}{2j-1}} \left(\frac{\mathrm{d}}{\mathrm{d}r} + \frac{j}{r}\right) u_{jm}^{j-1}, \tag{2.18}$$

$$\tau_{jm}^{j-1,2} = 2\mu\sqrt{\frac{j-1}{2(2j-1)}} \left(\frac{\mathrm{d}}{\mathrm{d}r} + \frac{j+1}{r}\right) u_{jm}^{j}, \tag{2.19}$$

$$\tau_{jm}^{j,2} = -2\mu\sqrt{\frac{(j+1)(2j+3)}{6(2j-1)(2j+1)}} \left(\frac{\mathrm{d}}{\mathrm{d}r} - \frac{j-1}{r}\right) u_{jm}^{j-1} +$$

$$+ 2\mu\sqrt{\frac{j(2j-1)}{6(2j+1)(2j+3)}} \left(\frac{\mathrm{d}}{\mathrm{d}r} + \frac{j+2}{r}\right) u_{jm}^{j+1}, \tag{2.20}$$

$$\tau_{jm}^{j+1,2} = -2\mu\sqrt{\frac{j+2}{2(2j+1)}} \left(\frac{\mathrm{d}}{\mathrm{d}r} - \frac{j}{r}\right) u_{jm}^{j}, \tag{2.21}$$

$$\tau_{jm}^{j+2,2} = -\sqrt{\frac{j+2}{2j+3}} \left(\frac{\mathrm{d}}{\mathrm{d}r} - \frac{j+1}{r}\right) u_{jm}^{j+1}. \tag{2.22}$$

The previous equations can also be simplified into the form

$$\tau_{jm}^{j-2,2} + A_5\frac{\mathrm{d}u_{jm}^{j-1}}{\mathrm{d}r} + A_6\frac{u_{jm}^{j-1}}{r} = 0, \tag{2.23}$$

15

$$\tau_{jm}^{j-1,2} + A_7 \frac{\mathrm{d}u_{jm}^j}{\mathrm{d}r} + A_8 \frac{u_{jm}^j}{r} = 0, \tag{2.24}$$

$$\tau_{jm}^{j,2} + A_9 \frac{\mathrm{d}u_{jm}^{j-1}}{\mathrm{d}r} + A_{10} \frac{u_{jm}^{j-1}}{r} + A_{11} \frac{\mathrm{d}u_{jm}^{j+1}}{\mathrm{d}r} + A_{12} \frac{u_{jm}^{j+1}}{r} = 0, \tag{2.25}$$

$$\tau_{jm}^{j+1,2} + A_{13} \frac{\mathrm{d}u_{jm}^j}{\mathrm{d}r} + A_{14} \frac{u_{jm}^j}{r} = 0, \tag{2.26}$$

$$\tau_{jm}^{j+2,2} + A_{15} \frac{\mathrm{d}u_{jm}^{j+1}}{\mathrm{d}r} + A_{16} \frac{u_{jm}^{j+1}}{r} = 0, \tag{2.27}$$

where the coefficients A_i are given in the table 2.1 on page 18 and they are only dependent on the value of the parameter j, hence they are constant for every individual value of j.

2.2.3 Equation of motion

In order to get the spectral form of the equation of motion 2.3, the divergence of the Cauchy stress tensor is required

$$\nabla \cdot \boldsymbol{\tau} = \sum_{j=0}^{\infty} \sum_{m=-j}^{j} \left[\nabla \cdot (\tau_{jm}^{j0} \mathbf{Y}_{jm}^{j0}) + \sum_{l=|j-2|}^{j+2} \nabla \cdot (\tau_{jm}^{l2} \mathbf{Y}_{jm}^{l2}) \right]. \tag{2.28}$$

Using the formula for the divergence of tensors stated e.g. in Golle et al. (2012), this can be rewritten in the spectral form

$$\nabla \cdot \boldsymbol{\tau} =$$

$$\sum_{j=0}^{\infty} \sum_{m=-j}^{j} -\sqrt{\frac{j}{3(2j+1)}} \left(\frac{\mathrm{d}}{\mathrm{d}r} + \frac{j+1}{r} \right) \tau_{jm}^{j0} \vec{Y}_{jm}^{j-1}$$

$$+ \sqrt{\frac{j+1}{3(2j+1)}} \left(\frac{\mathrm{d}}{\mathrm{d}r} - \frac{j}{r} \right) \tau_{jm}^{j0} \vec{Y}_{jm}^{j+1}$$

$$+ \sqrt{\frac{j-1}{3(2j-1)}} \left(\frac{\mathrm{d}}{\mathrm{d}r} - \frac{j-2}{r} \right) \tau_{jm}^{j-2,2} \vec{Y}_{jm}^{j-1}$$

$$- \sqrt{\frac{j-1}{2(2j+1)}} \left(\frac{\mathrm{d}}{\mathrm{d}r} - \frac{j-1}{r} \right) \tau_{jm}^{j-1,2} \vec{Y}_{jm}^{j} \tag{2.29}$$

$$- \sqrt{\frac{(j+1)(2j+3)}{6(2j+1)(2j-1)}} \left(\frac{\mathrm{d}}{\mathrm{d}r} + \frac{j+1}{r} \right) \tau_{jm}^{j2} \vec{Y}_{jm}^{j-1}$$

$$+ \sqrt{\frac{j(2j-1)}{6(2j+1)(2j+3)}} \left(\frac{\mathrm{d}}{\mathrm{d}r} - \frac{j}{r} \right) \tau_{jm}^{j2} \vec{Y}_{jm}^{j+1}$$

$$- \sqrt{\frac{j+2}{2(2j+1)}} \left(\frac{\mathrm{d}}{\mathrm{d}r} + \frac{j+2}{r} \right) \tau_{jm}^{j+1,2} \vec{Y}_{jm}^{j}$$

$$- \sqrt{\frac{j+2}{2j+3}} \left(\frac{\mathrm{d}}{\mathrm{d}r} + \frac{j+3}{r} \right) \tau_{jm}^{j+2,2} \vec{Y}_{jm}^{j+1}.$$

This gives us three equations

$$F_{jm}^{j-1} + A_{17}\frac{\mathrm{d}\tau_{\mathrm{jm}}^{j0}}{\mathrm{d}r} + A_{18}\frac{\tau_{jm}^{j0}}{r} + A_{19}\frac{\mathrm{d}\tau_{\mathrm{jm}}^{j-2,2}}{\mathrm{d}r} + A_{20}\frac{\tau_{jm}^{j-2,2}}{r} + A_{21}\frac{\mathrm{d}\tau_{\mathrm{jm}}^{j2}}{\mathrm{d}r} + A_{22}\frac{\tau_{jm}^{j2}}{r} = 0, \quad (2.30)$$

$$F_{jm}^{j} + A_{23}\frac{\mathrm{d}\tau_{\mathrm{jm}}^{j-1,2}}{\mathrm{d}r} + A_{24}\frac{\tau_{jm}^{j-1,2}}{r} + A_{25}\frac{\mathrm{d}\tau_{\mathrm{jm}}^{j+1,2}}{\mathrm{d}r} + A_{26}\frac{\tau_{jm}^{j+1,2}}{r} = 0, \quad (2.31)$$

$$F_{jm}^{j+1} + A_{27}\frac{\mathrm{d}\tau_{\mathrm{jm}}^{j0}}{\mathrm{d}r} + A_{28}\frac{\tau_{jm}^{j0}}{r} + A_{29}\frac{\mathrm{d}\tau_{\mathrm{jm}}^{j2}}{\mathrm{d}r} + A_{30}\frac{\tau_{jm}^{j2}}{r} + A_{31}\frac{\mathrm{d}\tau_{\mathrm{jm}}^{j+2,2}}{\mathrm{d}r} + A_{32}\frac{\tau_{jm}^{j+2,2}}{r} = 0, \quad (2.32)$$

where the coefficients A_i are given in the table 2.1 on page 18. The equations 2.30 and 2.32 match the spheroidal part of the equation of motion whereas Eq.2.31 is its toroidal part. In the thesis, it will be sufficient to use only the spheroidal parts as we are interested only in the radial component of motion.

2.2.4 Boundary condition

There is no external force $\vec{T}$ at the bottom of the shell in the most simple case. The equation (2.4) can then be rewritten in the form for the top boundary of the shell

$$\boldsymbol{\tau} \cdot \vec{e_r} + \rho g u_r \vec{e_r} = 0. \quad (2.33)$$

The product of the radial unit vector and the Cauchy stress tensor can be expressed in the spectral form, applying the formula from Matas (1995) as

$$\begin{aligned}
\boldsymbol{\tau} \cdot \vec{e_r} &= \vec{e_r} \sum_{jm}\sum_{lk} \tau_{jm}^{lk} Y_{jm}^{lk} = \\
&= \tau_{jm}^{j0}(A_{36}Y_{jm}^{j+1} + A_{33}Y_{jm}^{j-1}) + \tau_{jm}^{j-2,2}A_{34}Y_{jm}^{j-1} + \tau_{jm}^{j-1,2}A_{39}Y_{jm}^{j} + \\
&\quad + \tau_{jm}^{j2}(A_{37}Y_{jm}^{j+1} + A_{35}Y_{jm}^{j-1}) + \tau_{jm}^{j+1,2}A_{40}Y_{jm}^{j} + \tau_{jm}^{j+2,2}A_{38}Y_{jm}^{j+1},
\end{aligned} \quad (2.34)$$

where A_i coefficients are again in the table 2.1. If the whole expression is substituted into the Eq.(2.33) where u_r is supposed zero at this time, we can separate the vector equation according to the subscripts of the spherical harmonics

$$A_{33}\tau_{jm}^{j0} + A_{34}\tau_{jm}^{j-2,2} + A_{35}\tau_{jm}^{j2} = 0, \quad (2.35)$$

$$A_{36}\tau_{jm}^{j0} + A_{37}\tau_{jm}^{j2} + A_{38}\tau_{jm}^{j+2,2} = 0, \quad (2.36)$$

$$A_{39}\tau_{jm}^{j-1,2} + A_{40}\tau_{jm}^{j+1,2} = 0. \quad (2.37)$$

If u_r is non-zero it can be computed in spectral form using the formula from Matas (1995)

$$u_r = \vec{u} \cdot \vec{e_r} = \sum_{jm}\left(\sqrt{\frac{j}{2j+1}}u_{jm}^{j-1} - \sqrt{\frac{j+1}{2j+1}}u_{jm}^{j+1}\right)Y_{jm}. \quad (2.38)$$

where

$$u_r \vec{e}_r = \sum_{jm} \left(\sqrt{\frac{j}{2j+1}} u_{jm}^{j-1} - \sqrt{\frac{j+1}{2j+1}} u_{jm}^{j+1} \right) Y_{jm} \vec{e}_r =$$

$$= \sum_{jm} \left(\sqrt{\frac{j}{2j+1}} u_{jm}^{j-1} - \sqrt{\frac{j+1}{2j+1}} u_{jm}^{j+1} \right) \left(\sqrt{\frac{j}{2j+1}} Y_{jm}^{j-1} - \sqrt{\frac{j+1}{2j+1}} Y_{jm}^{j+1} \right) =$$

$$= \sum_{jm} \frac{j}{2j+1} u_{jm}^{j-1} Y_{jm}^{j-1} - \frac{\sqrt{j(j+1)}}{2j+1} (u_{jm}^{j-1} Y_{jm}^{j+1} + u_{jm}^{j+1} Y_{jm}^{j-1}) + \frac{j+1}{2j+1} u_{jm}^{j+1} Y_{jm}^{j+1}.$$

$$(2.39)$$

The last equation brings additional terms in the boundary equations decomposed in the spectral form in Eqs.(2.35) and (2.36).

A_i	Coefficient	A_i	Coefficient	A_i	Coefficient
A_1	$\sqrt{j}$	A_2	$-(j-1)\sqrt{j}$	A_3	$-\sqrt{j+1}$
A_4	$-(j+2)\sqrt{j+1}$	A_5	$-2\sqrt{\frac{j-1}{2j-1}}$	A_6	$-2j\sqrt{\frac{j-1}{2j-1}}$
A_7	$-2\sqrt{\frac{j-1}{2(2j+1)}}$	A_8	$-2(j+1)\sqrt{\frac{j-1}{2(2j+1)}}$	A_9	$2\sqrt{\frac{(j+1)(2j+3)}{6(2j-1)(2j+1)}}$
A_{10}	$-2(j-1)\sqrt{\frac{(j+1)(2j+3)}{6(2j-1)(2j+1)}}$	A_{11}	$-2\sqrt{\frac{j(2j-1)}{6(2j+3)(2j+1)}}$	A_{12}	$-2(j+2)\sqrt{\frac{j(2j-1)}{6(2j+3)(2j+1)}}$
A_{13}	$2\sqrt{\frac{j+2}{2(2j+1)}}$	A_{14}	$-2j\sqrt{\frac{j+2}{2(2j+1)}}$	A_{15}	$2\sqrt{\frac{j+2}{2j+3}}$
A_{16}	$-2(j+1)\sqrt{\frac{j+2}{2j+3}}$	A_{17}	$-\sqrt{\frac{j}{3(2j+1)}}$	A_{18}	$-(j+1)\sqrt{\frac{j}{3(2j+1)}}$
A_{19}	$\sqrt{\frac{j-1}{2j-1}}$	A_{20}	$-(j-2)\sqrt{\frac{j-1}{2j-1}}$	A_{21}	$-\sqrt{\frac{(j+1)(2j+3)}{6(2j-1)(2j+1)}}$
A_{22}	$-(j+1)\sqrt{\frac{(j+1)(2j+3)}{6(2j-1)(2j+1)}}$	A_{23}	$-\sqrt{\frac{j-1}{2(2j+1)}}$	A_{24}	$(j-1)\sqrt{\frac{j-1}{2(2j+1)}}$
A_{25}	$-\sqrt{\frac{j+2}{2(2j+1)}}$	A_{26}	$-(j+2)\sqrt{\frac{j+2}{2(2j+1)}}$	A_{27}	$\sqrt{\frac{j+1}{3(2j+1)}}$
A_{28}	$-j\sqrt{\frac{j+1}{3(2j+1)}}$	A_{29}	$\sqrt{\frac{j(2j-1)}{6(2j+1)(2j+3)}}$	A_{30}	$-j\sqrt{\frac{j(2j-1)}{6(2j+1)(2j+3)}}$
A_{31}	$-\sqrt{\frac{j+2}{2j+3}}$	A_{32}	$-(j+3)\sqrt{\frac{j+2}{2j+3}}$	A_{33}	$-\sqrt{\frac{j}{3(2j+1)}}$
A_{34}	$\sqrt{\frac{j-1}{2j-1}}$	A_{35}	$-\sqrt{\frac{(j+1)(2j+3)}{6(2j+1)(2j-1)}}$	A_{36}	$\sqrt{\frac{j+1}{3(2j+1)}}$
A_{37}	$\sqrt{\frac{j(2j-1)}{6(2j+1)(2j+3)}}$	A_{38}	$-\sqrt{\frac{j+2}{2j+3}}$	A_{39}	$\sqrt{\frac{j-1}{2(2j+1)}}$
A_{40}	$-\sqrt{\frac{j+2}{2(2j+1)}}$				

Table 2.1: Table of coefficients

2.3   Finite difference method

In order to achieve the numerical solution of the equations (2.1), (2.2), (2.3) and boundary condition (2.4), we use the finite difference method. This method transforms the differential equations in the spherical form (obtained in the previous section) into the system of algebraic equations.

The main advantage of this method is quite intuitive discretization of continuous variables. In this section we automatically suppose that each equation has its spectral counterparts (in the previous chapter denoted by j and m subscripts). From this point on, instead of subscripts j and m, another subscript i will be written which represents the separate layers of the spherical shells (j and m are still used but they are not as important for the discretization procedure). The superscripts are left unchanged in comparison to the previous section.

The indices are ordered in ascending order as the variables represent higher depths measured from the top of the shell. However, some variables that we are manipulating with are well defined only on the interfaces between every two layers due to our discrete derivatives. These variables are scalar and tensor variables. On the contrary, vector variables will be defined in the middle of the layers which is schematically shown in the Fig. 2.1. It is assumed these layers have non-zero thickness.
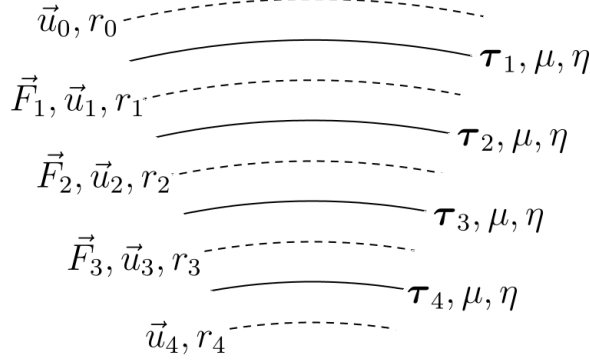

Figure 2.1: Scheme describing which variables are defined on the layers and which are in contrast defined on their interfaces.

In the decomposed governing equations, there is a need to define discrete derivatives. Note that in these equations there are only two kinds of terms. The first one contains $\frac{f}{r}$, the second one $\frac{\mathrm{d}f}{\mathrm{d}r}$, where f could be any continuous variable used in the previous sections. Using the finite difference method we can discretize these forms into the following forms

$$\frac{f}{r} = \frac{f_i + f_{i+1}}{r_i + r_{i+1}}, \tag{2.40}$$

$$\frac{\mathrm{d}f}{\mathrm{d}r} = \frac{f_i - f_{i-1}}{r_i - r_{i-1}}. \tag{2.41}$$

The governing equations (2.1)-(2.4) can be discretized using first the spectral decomposition and second the finite difference method as

$$A_1 \frac{u_i^{j-1} - u_{i-1}^{j-1}}{r_i - r_{i-1}} + A_2 \frac{u_i^{j-1} + u_{i-1}^{j-1}}{r_i + r_{i-1}} + A_3 \frac{u_i^{j+1} - u_{i-1}^{j+1}}{r_i - r_{i-1}} + A_4 \frac{u_i^{j+1} + u_{i-1}^{j+1}}{r_i + r_{i-1}} = 0, \tag{2.42}$$

$$\tau_i^{j-2,2} + A_5 \frac{u_i^{j-1} - u_{i-1}^{j-1}}{r_i - r_{i-1}} + A_6 \frac{u_i^{j-1} - u_{i-1}^{j-1}}{r_i + r_{i-1}} = 0, \tag{2.43}$$

$$\begin{aligned} \tau_i^{j,2} + A_9 \frac{u_i^{j-1} - u_{i-1}^{j-1}}{r_i - r_{i-1}} + A_{10} \frac{u_i^{j-1} - u_{i-1}^{j-1}}{r_i + r_{i-1}} + \\ + A_{11} \frac{u_i^{j+1} - u_{i-1}^{j+1}}{r_i - r_{i-1}} + A_{12} \frac{u_i^{j+1} - u_{i-1}^{j+1}}{r_i + r_{i-1}} = 0, \end{aligned} \tag{2.44}$$

$$\tau_i^{j+2,2} + A_{15} \frac{u_i^{j+1} - u_{i-1}^{j+1}}{r_i - r_{i-1}} + A_{16} \frac{u_i^{j+1} - u_{i-1}^{j+1}}{r_i + r_{i-1}} = 0, \tag{2.45}$$

$$A_{17}\frac{\tau_{i+1}^{j,0} - \tau_i^{j,0}}{\frac{r_{i+1}-r_{i-1}}{2}} + A_{18}\frac{\tau_{i+1}^{j,0} + \tau_i^{j,0}}{r_{i+1} + r_{i-1}} + A_{19}\frac{\tau_{i+1}^{j-2,2} - \tau_i^{j-2,2}}{\frac{r_{i+1}-r_{i-1}}{2}} + A_{20}\frac{\tau_{i+1}^{j-2,2} + \tau_i^{j-2,2}}{r_{i+1} + r_{i-1}} +$$

$$+ A_{21}\frac{\tau_{i+1}^{j,2} - \tau_i^{j,2}}{\frac{r_{i+1}-r_{i-1}}{2}} + A_{22}\frac{\tau_{i+1}^{j,2} + \tau_i^{j,2}}{r_{i+1} + r_{i-1}} = F_i^{j-1},$$

$$(2.46)$$

$$A_{27}\frac{\tau_{i+1}^{j,0} - \tau_i^{j,0}}{\frac{r_{i+1}-r_{i-1}}{2}} + A_{28}\frac{\tau_{i+1}^{j,0} + \tau_i^{j,0}}{r_{i+1} + r_{i-1}} + A_{29}\frac{\tau_{i+1}^{j,2} - \tau_i^{j,2}}{\frac{r_{i+1}-r_{i-1}}{2}} + A_{30}\frac{\tau_{i+1}^{j,2} + \tau_i^{j,2}}{r_{i+1} + r_{i-1}} +$$

$$+ A_{31}\frac{\tau_{i+1}^{j+2,2} - \tau_i^{j+2,2}}{\frac{r_{i+1}-r_{i-1}}{2}} + A_{32}\frac{\tau_{i+1}^{j+2,2} + \tau_i^{j+2,2}}{r_{i+1} + r_{i-1}} = F_i^{j+1},$$

$$(2.47)$$

$$A_{33}\tau_i^{j,0} + A_{34}\tau_i^{j-2,2} + A_{35}\tau_i^{j,2} = 0, \qquad (2.48)$$

$$A_{36}\tau_i^{j,0} + A_{37}\tau_i^{j,2} + A_{38}\tau_i^{j+2,2} = 0, \qquad (2.49)$$

where A_k are the constant values given by the specified value of j for all $k \in \{1,...,40\}$ available in the table 2.1 on page 18. In boundary conditions there are omitted terms coming from the second term of 2.4 in order to simplify the notation.

2.4   Linear algebraic equations solution

Let us rewrite the equations derived in the section 2.3 into the matrix form. For the sake of making the computation simple, there is an urge to arrange them with an emphasis to keep the matrix in a band form. We write the equations in the following order: Equation of continuity, rheological equations, equations of motion. The equations of motion are computed in the middle of the mantle's layers and thus there is one less pair of these equations. Instead of the equation of motion we use, therefore, the boundary equations on the boundaries of the spherical shell. These two pairs of the boundary conditions are represented by the first and the second row of the matrix both from the top and from the bottom. The matrix is therefore structured the following way

$$A_j = \begin{pmatrix} \text{(2 rows)} & \text{Top boundary condition} \\ & \left\{ \begin{array}{l} \text{(1 row) Continuity equation} \\ \text{(3 rows) Rheological relationship} \\ \text{(2 rows) Equation of motion} \end{array} \right. \\ \text{(1 row)} & \text{Continuity equation} \\ \text{(3 rows)} & \text{Rheological relationship} \\ \text{(2 rows)} & \text{Bottom boundary condition} \end{pmatrix}, \qquad (2.50)$$

where n is the number of interfaces between the layers ($n-1$ is the number of layers). It makes altogether $6n+2$ equations. Nevertheless, if there are $6n+2$ equations in the scheme, we are able to solve them for $6n+2$ variables.

Let us take a closer look on the variables we are interested in. We suppose the force is exogenous, hence it will constitute the vector of the right hand side $\vec{b}_{jm}$, and thus it is not involved in the solved matrix A_j. The remaining variables which

can be obtained are variables $\boldsymbol{\tau}$ and $\vec{u}$. The total number of these variables, if we reflect the spectral decomposition, is nine for every layer i (respectively interface between the layers) which are namely u_i^{j-1}, u_i^j, u_i^{j+1}, τ_i^{j0}, $\tau_i^{j-2,2}$, $\tau_i^{j-1,2}$, τ_i^{j2}, $\tau_i^{j+1,2}$, $\tau_i^{j+2,2}$.

However, three of these variables are toroidal (i.e. they influence only the non-radial component of the displacement or the stress of the planet) and we can exclude them. This exclusion leaves us with only six variables which are, on the other hand, sferoidal (i.e. they influence the radial component of the studied variables, and thus are important for the matrix solution). The three toroidal variables excluded are $u_i^j, \tau_i^{j-1,2}, \tau_i^{j-1,2}$.

Thereafter we have six variables for every set of the equations and thus match the $6n$ in the matrix above. The remaining two equations handle the additional two variables u_i^{j-1} and u_i^{j+1} because there is an extra pair due to the fact that the displacement is in the discretized model defined on the interfaces between the layers (see Fig. 2.1 on page 19).

After the discretization done in section 2.3 we obtain exact forms of the equations which are put afterward in the matrix A. In order to make the notation more simple we introduce $\hat{r}_i = r_i + r_{i-1}$, $\hat{\hat{r}}_i = r_i + r_{i-2}$, $\tilde{r}_i = r_i - r_{i-1}$, $\tilde{\tilde{r}}_i = \frac{r_i - r_{i-2}}{2}$ The matrix equation which is to be solved is a simple algebraic equation in a form

$$A_j \vec{x}_{jm} = \vec{b}_{jm}, \tag{2.51}$$

where the vector of variables we are interested in is the vector $\vec{x}_{jm}$, A_j is the matrix for the specified spectral parameter j and $\vec{b}_{jm}$ is the vector of the right hand side which is composed of the external forces and will be discussed later. In the following matrix equation there is an indication of how the particular matrix cells are filled in (after pluging in the equations derived in the section 2.3).

$$
\begin{pmatrix}
0 & 0 & A_{34} & A_{35} & A_{32} & 0 & 0 & 0 & \cdots \\
0 & 0 & 0 & A_{37} & A_{36} & A_{38} & 0 & 0 & \cdots \\
\frac{(-\hat{r}_1 A_1 + \tilde{r}_1 A_2)}{\tilde{r}_1 \hat{r}_1} & \frac{(-\hat{r}_1 A_3 + \tilde{r}_1 A_4)}{\tilde{r}_1 \hat{r}_1} & 0 & 0 & 0 & 0 & \frac{(\hat{r}_1 A_1 + \tilde{r}_1 A_2)}{\tilde{r}_1 \hat{r}_1} & \frac{(\hat{r}_1 A_3 + \tilde{r}_1 A_4)}{\tilde{r}_1 \hat{r}_1} & \cdots \\
\frac{(-\hat{r}_1 A_5 + \tilde{r}_1 A_6)}{\tilde{r}_1 \hat{r}_1} & 0 & 1 & 0 & 0 & 0 & \frac{(\hat{r}_1 A_5 + \tilde{r}_1 A_6)}{\tilde{r}_1 \hat{r}_1} & 0 & \cdots \\
\frac{(-\hat{r}_1 A_9 + \tilde{r}_1 A_{10})}{\tilde{r}_1 \hat{r}_1} & \frac{(-\hat{r}_1 A_{11} + \tilde{r}_1 A_{12})}{\tilde{r}_1 \hat{r}_1} & 0 & 1 & 0 & 0 & \frac{(\hat{r}_1 A_9 + \tilde{r}_1 A_{10})}{\tilde{r}_1 \hat{r}_1} & \frac{(\hat{r}_1 A_{11} + \tilde{r}_1 A_{12})}{\tilde{r}_1 \hat{r}_1} & \cdots \\
0 & \frac{(-\hat{r}_1 A_{15} + \tilde{r}_1 A_{16})}{\tilde{r}_1 \hat{r}_1} & 0 & 0 & 1 & 0 & 0 & \frac{(\hat{r}_1 A_{15} + \tilde{r}_1 A_{16})}{\tilde{r}_1 \hat{r}_1} & \cdots \\
0 & 0 & \frac{(-\hat{r}_2 A_{19} + \tilde{r}_2 A_{20})}{\tilde{r}_2 \hat{r}_2} & \frac{(-\hat{r}_2 A_{21} + \tilde{r}_2 A_{22})}{\tilde{r}_2 \hat{r}_2} & \frac{(-\hat{r}_2 A_{17} + \tilde{r}_2 A_{18})}{\tilde{r}_2 \hat{r}_2} & 0 & 0 & 0 & \cdots \\
0 & 0 & 0 & \frac{(-\hat{r}_2 A_{29} + \tilde{r}_2 A_{30})}{\tilde{r}_2 \hat{r}_2} & \frac{(-\hat{r}_2 A_{27} + \tilde{r}_2 A_{28})}{\tilde{r}_2 \hat{r}_2} & \frac{(-\hat{r}_2 A_{31} + \tilde{r}_2 A_{32})}{\tilde{r}_2 \hat{r}_2} & 0 & 0 & \cdots \\
\vdots & \vdots & \vdots & \vdots & \vdots & \vdots & \vdots & \vdots & \ddots
\end{pmatrix}
\begin{pmatrix}
u_0^{j-1} \\
u_0^{j+1} \\
\tau_1^{j-2,2} \\
\tau_1^{j2} \\
\tau_1^{j0} \\
\tau_1^{j+2,2} \\
u_1^{j-1} \\
u_1^{j+1} \\
\vdots
\end{pmatrix}
= \vec{b}_{jm},
$$

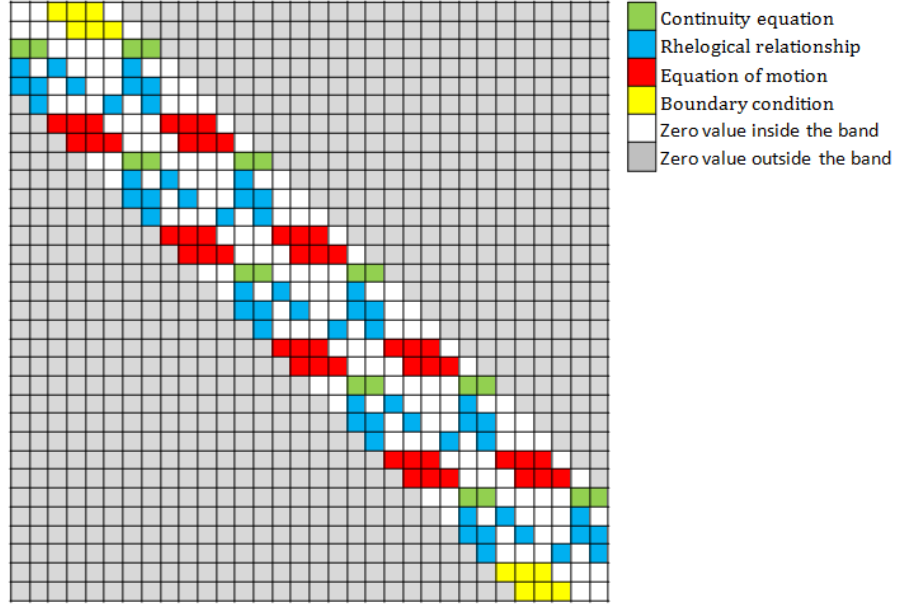The Figure 2.2 shows the non-zero elements of the matrix A_j for $n = 5$.

Figure 2.2: Scheme depicting non-zero elements and the band structure of the matrix A_j for $n = 5$ with omitting the terms caused by non-zero u_r in the boundary condition.

2.5 Maxwell rheology implementation

Until this moment, all equations in this chapter were describing a purely elastic model with no time dependency. Let us now adjust the elastic model presented on the previous pages and implement the Maxwell rheology in the spherical model. The most important change is in describing the functional form of the governing equations.

The continuity equation stays unchanged therefore we only restate it (c.f. Eq.(2.1))

$$\nabla \cdot \vec{u} = 0.$$

The equation of motion stays unchanged, too (c.f. Eq.(2.3))

$$-\nabla p + \nabla \cdot \mathbf{D} + \rho \vec{f} = 0,$$

The only governing equation which changes is the rheological relationship. We devote the following subsection to the derivation of the rheological relationship for the Maxwell model.

2.5.1 Rheological relationship for the Maxwell model

We examined relatively thoroughly the Maxwell model in chapter 1. The key equation which we need to implement is the Eq.(1.6) which we restate here

$$\dot{\varepsilon} = \frac{\sigma}{2\eta} + \frac{\dot{\sigma}}{2\mu}.$$

Since we assume that the shear modulus μ and the viscosity η are constant in a time, and the stress σ can be replaced by the deviatoric part $\mathbf{D}$ of the stress

tensor $\boldsymbol{\tau}$, we obtain the following equation

$$\frac{\dot{\mathbf{D}}}{2\mu} - \dot{\boldsymbol{\varepsilon}} = -\frac{\mathbf{D}}{2\eta}, \tag{2.52}$$

The strain $\boldsymbol{\varepsilon}$ can be replaced by the remaining part of the rheological relationship known from the elastic model, namely

$$\boldsymbol{\varepsilon} = \nabla\vec{u} + (\nabla\vec{u})^T. \tag{2.53}$$

Taking the time derivative and substituting the Eq.(2.53) into the Eq.(1.6)

$$\dot{\mathbf{D}} - 2\mu(\nabla\dot{\vec{u}} + (\nabla\dot{\vec{u}})^T) = -\frac{\mu}{\eta}\mathbf{D}. \tag{2.54}$$

It is important to state that the displacement u has to be relatively small in order to obtain an assumption that there is no advection term in the time derivative of the displacement. The advection term is the second term in the following equation

$$\dot{\vec{u}} = \frac{\partial\vec{u}}{\partial t} + \vec{u} \cdot \nabla\vec{u}. \tag{2.55}$$

In order to keep the mathematical background derived for the elastic model as similar to this as possible, we integrate Eq.(2.54) with respect to time and obtain

$$\mathbf{D} - 2\mu(\nabla\vec{u} + (\nabla\vec{u})^T) = -\frac{\mu}{\eta}\int_0^t \mathbf{D}dt'. \tag{2.56}$$

Let us now discretize this equation using 'the trapezoidal rule' which transforms continuous integrals to a discrete sums.

$$\mathbf{D}_{n+1} - 2\mu(\nabla\vec{u}_{n+1} + (\nabla\vec{u}_{n+1})^T) = -\frac{\mu}{\eta}\Delta t \sum_{i=0}^{n} \frac{\mathbf{D}_{i+1} + \mathbf{D}_i}{2}. \tag{2.57}$$

From this equation it is notable we need to know all previous values of the deviatoric stress $\mathbf{D}$ in order to count another one. In order to do so, we have to rearrange the term containing $\mathbf{D}_{n+1}$ on the right-hand-side, and thus make clear the pattern how to get the next D_{n+1} when we know all D_i where $i < n+1$. The pattern is derived in the following equation simply by rearranging a term from the sum in the Eq.(2.57).

$$\mathbf{D}_{n+1}\left(1 + \frac{\mu}{\eta}\frac{\Delta t}{2}\right) - 2\mu(\nabla\vec{u}_{n+1} + (\nabla\vec{u}_{n+1})^T) = -\frac{\mu}{\eta}\Delta t\left(\frac{\mathbf{D}_0}{2} + \sum_{i=1}^{n}\mathbf{D}_i\right). \tag{2.58}$$

This is the final form of the rheological relationship for the Maxwell model discretized in time. If we would like to discretize it also in the spatial dimension similarly as in the elastic case, the obtained equation is changed in comparison to the elastic case only in two details. First, that there is some constant factor multiplying the stress variables, which changes the matrix A_j to a new matrix (similar though), say B_j. Second, that there exists a term which has to be put in

the right-hand-side vector. The solution for this model by solving gradually the following set of matrix equations

$$B_j \vec{x}_{jm}^0 = \vec{b}_{jm}^0,$$
$$B_j \vec{x}_{jm}^1 = \vec{b}_{jm}^1,$$
$$\vdots$$
$$B_j \vec{x}_{jm}^n = \vec{b}_{jm}^n,$$

(2.59)

where the superscripts denote the indices of a time discretization. $\vec{b}_{jm}^i$ can be obtained from the $\vec{x}_{jm}^{i-1}$ simply according to the right-hand-side in Eq.(2.58). The important thing which makes the computation sustainable is the fact that the matrix B_j does not depend on time, which means that it is sufficient to compute it only once and then only change vectors of the right-hand-side. Numerical solution of the large matrices we use will be discussed later.

2.6 Kelvin-Voigt rheology implementation

Similarly as in the Maxwell model, the continuity equation stays the same as in the elastic model (c.f. Eq.(2.1))

$$\nabla \cdot \vec{u} = 0, ,$$

(2.1)

as well as the equation of motion

$$\nabla \cdot \boldsymbol{\tau} + \vec{f} = 0.$$

(2.3)

The only difference in the model lies in the fact that the rheological relationship is different which will be focused on in the following subsection.

2.6.1 Rheological relationship for the Kelvin-Voigt model

We examined relatively thoroughly the Kelvin-Voigt model in chapter 1 as well as the Maxwell model. The key equation which we need to implement this time is the Eq.(1.13) which we restate here

$$\sigma = 2\eta\dot{\varepsilon} + 2\mu\varepsilon.$$

(1.13)

Since we again assume that the shear modulus μ and the viscosity η are constant in time, and the stress σ can be replaced by the deviatoric part $\mathbf{D}$ of the stress tensor $\boldsymbol{\tau}$, we obtain the following equation, where bold $\boldsymbol{\varepsilon}$ symbolizes strain tensor

$$\mathbf{D} - 2\mu\boldsymbol{\varepsilon} = 2\eta\dot{\boldsymbol{\varepsilon}}.$$

(2.60)

This equation can be discretized using the discrete derivative according to the following formula

$$\frac{\mathrm{d}\boldsymbol{\varepsilon}}{\mathrm{d}t} = \frac{\boldsymbol{\varepsilon}_{n+1} - \boldsymbol{\varepsilon}_n}{\Delta t},$$

(2.61)

resulting in

$$\mathbf{D}_{n+1} - 2\mu\boldsymbol{\varepsilon}_{n+1} = 2\eta\frac{\boldsymbol{\varepsilon}_{n+1} - \boldsymbol{\varepsilon}_n}{\Delta t},$$

(2.62)

where Δt is a time discretization step. This equation can be rearranged

$$\mathbf{D}_{n+1} - 2\left(\mu + \frac{\eta}{\Delta t}\right)\varepsilon_{n+1} = -2\eta\frac{\varepsilon_n}{\Delta t}, \tag{2.63}$$

This is the final form of the rheological relationship for the Kelvin-Voigt model discretized in time similarly as Eq.2.58 was for the Maxwell model. If we would like to discretize it also in the spatial dimension, the obtained equation is in comparison to the elastic case changed again in two details, but slightly different than in the case of Maxwell model. First, there is a constant factor multiplying the strain variables (in Maxwell model it was stress). This detail changes the matrix A_j to a new matrix C_j (similar to both elastic A_j and Maxwell B_j). Second detail is that there exists a term which has to be put in the right-hand-side vector. This time, however, the right-hand-side depends only on the term preceding the current step, not on all the terms as in case of the Maxwell model. It means that it is sufficient to know variables from the previous step and the solution for the current step can be found. The solution for this model is again found by solving a set of matrix equations

$$\begin{aligned} C_j\vec{x}_{jm}^0 &= \vec{b}_{jm}^0, \\ C_j\vec{x}_{jm}^1 &= \vec{b}_{jm}^1, \\ &\vdots \\ C_j\vec{x}_{jm}^n &= \vec{b}_{jm}^n, \end{aligned} \tag{2.64}$$

where the superscripts denote the indices of a time discretization. $\vec{b}_{jm}^i$ can be obtained from the $\vec{x}_{jm}^{i-1}$ similarly as in the case of Maxwell model according to the right-hand-side in Eq.(2.63). The important thing which makes the computation sustainable is the fact that the matrix C_j does not depend on the time in the same way it does not depend in case of Maxwell. Therefore, the computation can be done only once and only variable which changes is the vector b_{jm}^i.

2.7 Tidal potential

The tidal deformations have long been studied by physicists and astronomists as a way to describe the change in shape of the planetary and satellite surface, especially atmospheres and oceans. Johannes Kepler suggested already in the seventeenth century in his Astronomica Nova (1609) that the Moon causes tides and ebbs. Followed by Galileo Galilei, Newton and Laplace the theory of tides extended significantly.

Tidal heating, a process caused by the tidal deformations and frictions, is regarded as one of the possible sources of the energy of some of the planetary bodies in the Solar System. Thermal heating budget for various satellites in the Solar System is shown by Chen et al. (2014) where they show that e.g. in case of Jupiter's satellite Europa or Saturn's satellite Enceladus there is much higher contribution of solid body eccentricity tidal heating than in case of other satellites which heats are mostly generated by radiogenic heating caused by the fission of radioactive materials.

The motivation is therefore to adjust the models used in this thesis for the tidal heating due to their eccentricity. The key how to implement it to the equations that have been already derived is via the so called tidal potential.

The equation for the boundary condition introduced previously can be extended for the presence of the external force given by the tidal potential. The functional form of the equation will then be

$$\tau \cdot \vec{e_r} - u_r \Delta \rho g \vec{e_r} = -\rho_{core} \ \varphi \vec{e_r}, \tag{2.65}$$

where $\Delta \rho$ is the difference between the density of the shell ρ_{shell} and the density of the core ρ_{core} of the studied planetary body and φ is the tidal potential. The tidal potential for a synchronous eccentric orbit with a time variation is given e.g. by Kaula (1964) or Moore & Schubert (2000):

$$\varphi(r, \theta, \phi) = r^2 \omega^2 e \left\{ -\tfrac{3}{2} P_2^0 (\cos \theta) \cos \omega t + \tfrac{1}{4} P_2^2 (\cos \theta) \left[3 \cos \omega t \cos 2\phi + 4 \sin \omega t \sin 2\phi \right] \right\}, \tag{2.66}$$

where P_2^0 and P_2^2 are the associate Legendre functions, e is the eccentricity of the planetary body, ω is the angular frequency and r, θ and φ are spherical coordinates. In order to change this equation in the spherical form, we need to transform the associate Legendre functions in the form of spherical harmonics. The linking formula between these two mathematical functions is as follows

$$Y_{jm}(\theta, \phi) = (-1)^m N_{jm} P_{jm}(\cos \theta) e^{im\phi}, \tag{2.67}$$

where

$$N_{jm} = \left[\frac{(2j+1)(j-m)!}{4\pi(j+m)!} \right]. \tag{2.68}$$

In case of Legendre function $P_2^0 (\cos \theta)$ as in the first term of Eq.(2.66), the Eq.2.67 transforms into

$$P_2^0 (\cos \theta) = \frac{Y_{20}(\theta, \phi)}{N_{20}}. \tag{2.69}$$

For the rest Legendre functions Eq.(2.67) can be rewritten using the following identities

$$\cos 2\phi = \frac{e^{2i\phi} + e^{-2i\phi}}{2}, \tag{2.70}$$

$$\sin 2\phi = \frac{e^{2i\phi} - e^{-2i\phi}}{2i}, \tag{2.71}$$

as

$$Y_{22} + Y_{2-2} = 2N_{22} P_2^2 (\cos \theta) \cos 2\phi, \tag{2.72}$$

$$Y_{22} - Y_{2-2} = 2N_{22} P_2^2 (\cos \theta) \sin 2\phi, \tag{2.73}$$

and by rearranging we obtain

$$\cos 2\phi = \frac{Y_{22} + Y_{2-2}}{2N_{22} P_2^2 (\cos \theta)}, \tag{2.74}$$

$$\sin 2\phi = \frac{Y_{22} + Y_{2-2}}{2i N_{22} P_2^2 (\cos \theta)}. \tag{2.75}$$

After substitution of Eqs.(2.69), (2.74) and (2.75) into Eq.(2.66) we obtain

$$\varphi(r, \theta, \phi) = r^2\omega^2 e \left\{ -\frac{3}{2}\cos\omega t \frac{Y_{20}}{N_{20}} + \left(\frac{3}{4}\cos\omega t \frac{Y_{22}+Y_{2-2}}{2N_{22}}\right) + \left(\sin\omega t \frac{Y_{22}-Y_{2-2}}{2iN_{22}}\right) \right\},$$
(2.76)

where after plugging the constants in the formula (2.68) we get

$$N_{22} = \sqrt{\frac{5}{96\pi}},$$
(2.77)

$$N_{20} = \sqrt{\frac{5}{4\pi}},$$
(2.78)

$$N_{2-2} = \sqrt{\frac{30}{\pi}},$$
(2.79)

and the Eq.(2.76) finally simplifies to

$$\varphi(r, \theta, \phi) = r^2\omega^2 e \left(-\sqrt{\frac{9\pi}{5}}\cos\omega t Y_{20} + \sqrt{\frac{27\pi}{10}}\cos\omega t Y_{22} - \sqrt{\frac{24\pi}{5}}i\sin\omega t Y_{22} + \right.$$
$$\left. +\sqrt{\frac{27\pi}{10}}\cos\omega t Y_{2-2} + \sqrt{\frac{24\pi}{5}}i\sin\omega t Y_{2-2} \right).$$
(2.80)

In order to find the form of the force $\vec{f}$ in the equation of motion (2.3), we will need to derive also a gradient of the tidal potential. If we define this force $\vec{f}$ as a tidal force, the formula for its computation is then

$$\vec{f} = \rho\nabla\varphi.$$
(2.81)

Therefore, there is an urge to find a gradient of the tidal potential which can be derived according formula in Matas (1995),

$$\nabla f(r) = \sum_{m\in\{-2,0,2\}} \left[\sqrt{\frac{2}{5}}\left(\frac{\mathrm{d}}{\mathrm{d}r} + \frac{3}{r}\right)f_{2m}(r)Y_{2m}^1 - \sqrt{\frac{3}{5}}\left(\frac{\mathrm{d}}{\mathrm{d}r} - \frac{2}{r}\right)f_{2m}(r)Y_{2m}^3 \right],$$
(2.82)

where $f(r)$ is any scalar function. If applied on the tidal potential the following equation is obtained because the second term factors out

$$\nabla\varphi(r, \theta, \phi) = r\omega^2 e(-\sqrt{18\pi}\cos\omega t Y_{20}^1 + \sqrt{27\pi}\cos\omega t Y_{22}^1 - \sqrt{48\pi}i\sin\omega t Y_{22}^1 + $$
$$ + \sqrt{27\pi}\cos\omega t Y_{2-2}^1 + \sqrt{48\pi}i\sin\omega t Y_{2-2}^1).$$
(2.83)

The gradient of the tidal potential can be substituted into the equation (2.81) and the following equation is obtained

$$\vec{f} = \rho\, r^2\omega^2 e \left\{ -\frac{3}{2}\cos\omega t \frac{Y_{20}}{N_{20}} + \left(\frac{3}{4}\cos\omega t \frac{Y_{22}+Y_{2-2}}{2N_{22}}\right) + \left(\sin\omega t \frac{Y_{22}-Y_{2-2}}{2iN_{22}}\right) \right\}.$$
(2.84)

3. Results

There is a number of planetary bodies in the Solar System which are interesting in terms of the source of their heat. Amongst them there might be, as previously stated, Saturn's ice satellite Enceladus as well as Jupiter's Europa. There might also occur a tidal deformation in bodies of higher density such as various exoplanets and specifically a silicate planet Mercury. All examined bodies are stated in Table 3.1 together with their parameters used in this thesis. There are two possible widths of mantle of Enceladus investigated as can be noticed in the mentioned table. In case of exoplanets there is in four cases the same setup as the exoplanet is imaginary choosing the parameter to be similar to Earth differentiating only in the orbital period which helps us identify the effect of the orbital period on the quality of the models. The parameters in the table for Enceladus were taken from Tobie et al. (2008), for Europa from Chen et al. (2014), and for Mercury from Balogh & Giampieri (2002) and some of them were slightly changed.

Planetary body	$g_{surface}$	g_{core}	ρ_{core}	ρ_{mantle}	e	T	r_{top}	r_{bottom}	μ
	$m \cdot s^{-2}$	$m \cdot s^{-2}$	$kg \cdot m^{-3}$	$kg \cdot m^{-3}$		$days$	km	km	GPa
Enceladus(26 km)	0.11	0.13	925	1007	0.0045	1.370	252.1	226.1	3.3
Enceladus(52 km)	0.11	0.13	925	1007	0.0045	1.370	252.1	200.1	3.3
Europa	1.31	1.31	925	1007	0.0090	3.551	1561.0	1531.0	3.3
Exoplanet(1 day)	9.73	10.74	4500	12000	0.1	1.000	6400.0	3200.0	70
Exoplanet(5 days)	9.73	10.74	4500	12000	0.1	5.000	6400.0	3200.0	70
Exoplanet(20 days)	9.73	10.74	4500	12000	0.1	20.000	6400.0	3200.0	70
Exoplanet(50 days)	9.73	10.74	4500	12000	0.1	50.000	6400.0	3200.0	70
Mercury	3.70	3.70	4000	7000	0.2	87.969	2450.0	2050.0	70

Table 3.1: Table of planetary bodies' parameters

3.1 Numerical implementation

The numerical implementation has been done in Fortran exactly according the mathematical model in the chapter 2. The correctness of the deformation was tested against the similar program of O. Čadek in case of Maxwell rheology. In case of the Kelvin-Voigt model the program was implemented similarly as for Maxwell model but tested against the theoretical property that the limit value for low viscosities goes to the elastic limit for all computed figures. For all results the computations are done at spectral degree $j = 2$.

There are three figures for every planetary body examined and in every figure there are depicted values modeled by Maxwell rheology and also by Kelvin-Voigt rheology. The first of the figures shows an amplitude of the radial displacement at the top of the mantle. The displacement is caused as was stated in chapter 2 by tidal and hydrostatic forces. The second depicts how the phase of the displacement maxima changes in comparison to the reference elastic case (in elastic case the phase offset is equal to zero). The third figure illustrates a heating power of the planet as it releases a significant portion of tidal heating.

Mathematically speaking, the first figure is depicting the maximal amplitude of radial displacement for given viscosity and is calculated exactly according Eq.2.38. The values in the second figure are calculated by measuring the os-

cillations phase offset of the maximal radial displacement amplitude. The last figure is calculated according the discretized version of Eqs.1.28 and 1.29.

3.2 Icy moons

Both icy moons examined in the thesis are assumed to have the same density parameters, i.e. their mantle and core are made of the same material as in case of the other moon. The values of these and the rest of parameters used were stated in Table 3.1 above. Even though the real bodies have also a rocky core under the subsurface ocean, we assume there is only water everywhere beneath the mantle.

3.2.1 Enceladus

Saturn's moon Enceladus is interesting due to its major source of energy via tidal heating and only negligible fraction of energy from the radiogenic source as stated in Chen et al. (2014). Therefore, the effect of tidal heating should be really significant in this case. Practically in all following figures there is a noticeable difference in the values for Maxwell and Kelvin-Voigt model. The first three figures are referring to Enceladus characterized by 26 km width of mantle whereas the second three figures shows Enceladus characterized by 52 km width of mantle.

In the Fig. 3.1 there are two curves denoting the decadic logarithm of an amplitude of the radial displacement on the surface of the mantle. It can be seen that Maxwell curve is for all values of viscosity above the Kelvin-Voigt model and thus generally predicts much higher displacement. The point where two models are the most similar to each other is when the viscosity is about 10^{14} Pa s. Whilst for low values of viscosity both models have finite non-zero limits, for the high values of viscosity the Kelvin-Voigt model is approaching zero as viscosity grows. If we limited the viscosity in Eqs.(2.58) and (2.63) from chapter 2, we would obtain (in the low viscosity case) the equation not depending on the change of the displacement in case of Maxwell and a reduction to a purely elastic case in Kelvin-Voigt model, and thus approaching an elastic limit. On the other hand, if the viscosity was high, the radial displacement amplitude would reach zero value for Kelvin-Voigt model and an elastic limit for the Maxwell model as the terms depending on viscosity are negligible in Eq.(2.58), which eliminates all the terms except for those present in the elastic model.

Let us take a closer look on what is the phase offset of the radial displacement in comparison to the purely elastic case. In the Fig. 3.2 the limits are consistent with the previous figure, i.e. Maxwell curve does not depend on the change of the displacement causing not changing the phase offset of the radial displacement for low values of viscosity and similarly there is obvious transition to the elastic limit in case of high viscosity. Interestingly, there is a peak around the viscosity 10^{13} Pa s, which is the value for which the other terms of Eq.(2.58) are not negligible, and therefore it creates a link between the viscosity and the radial displacement and its phase offset. Unlike the Maxwell model, according to Kelvin-Voigt model there is no phase offset peak. It is noticeable that for the low values of viscosity the curve reaches an elastic limit, i.e. zero phase offset. Curiously, the phase offset for high values of viscosity is different than Maxwell and is exactly $\frac{\pi}{2}$ radians

offset. The sharp increase in the phase offset occurs around the values of viscosity between 10^{13} Pa s and 10^{15} Pa s.

In the figure 3.3, a heating power created by the tidal forces on Enceladus is depicted. Although the peak power is above 10 GW around the viscosity value 10^{12} Pa s for the Maxwell model, the power predicted by the Kelvin-Voigt model is much less. In its maximum around the viscosity 10^{14} Pa s the power is approximately 0.3 GW which is about 30 times smaller than in case of Maxwell model. However, the values predicted by Maxwell are much higher only for lower viscosities than 10^{14} Pa s. Elsewhere, both predictions are the same and the power is gradually decreasing as the viscosity increases, which means the body is less liquid and thus the effect of tidal forces diminishes.
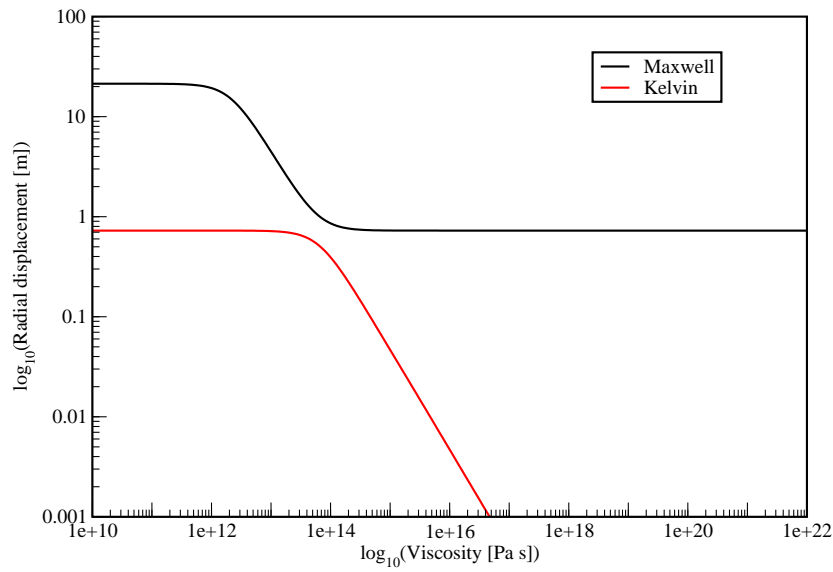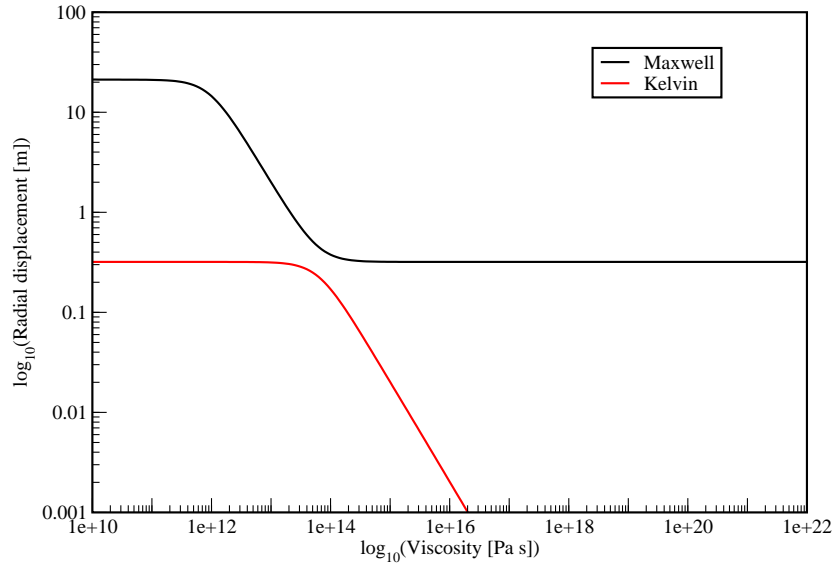

Figure 3.1: Enceladus - Radial displacement (26 km width)
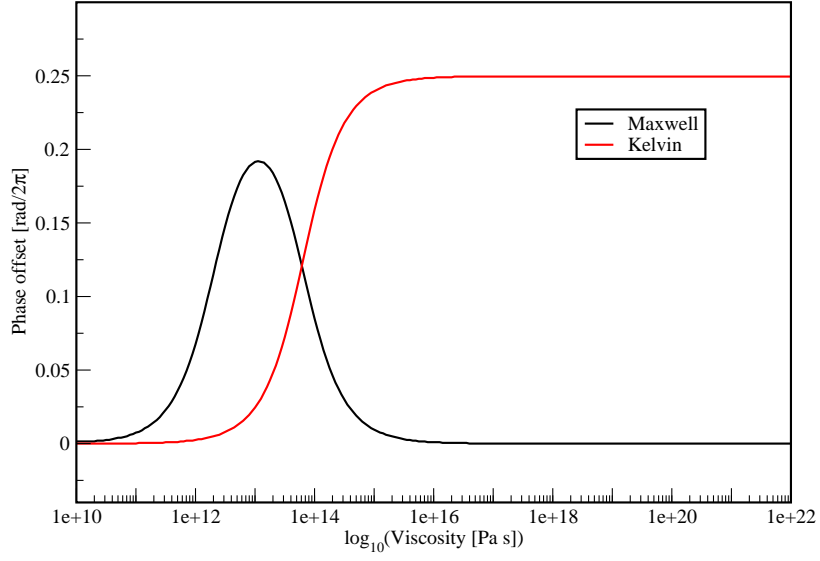
Figure 3.2: Enceladus - Phase offset (26 km width)
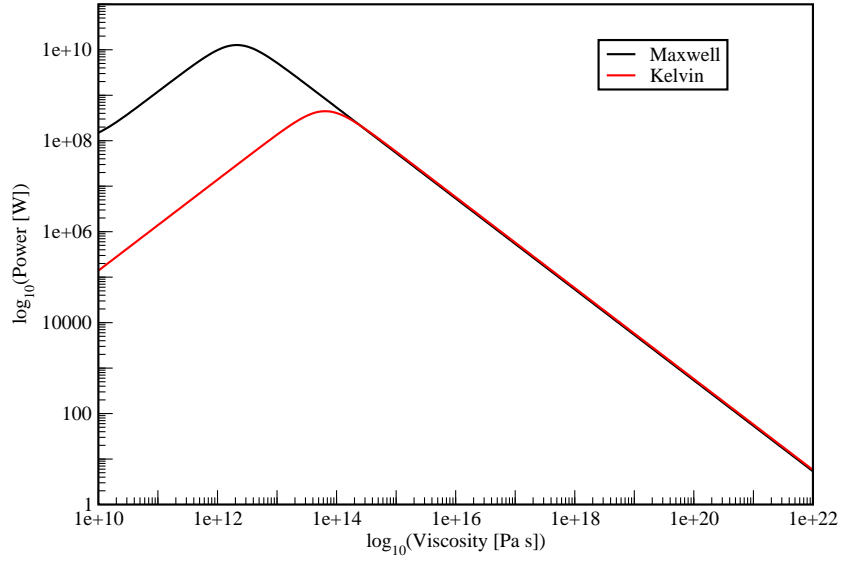
Figure 3.3: Enceladus - Power (26 km width)

In the Figs. 3.4, 3.5 and 3.6, there is no difference in the input parameters except for the width of the mantle and thus controlling for its specific effect. The radial displacement as can be seen in Fig.3.4, has not changed dramatically, the only difference is that there is a slight fall in the value representing the elastic limit. The rest of characteristics remains the same as stated in case of 26 km width of the mantle.

The Figure 3.5 regarding the phase offset changed only a bit in comparison to the smaller width of the mantle. The Kelvin-Voigt curve has not changed at all, however, the Maxwell curve increased a bit for the lower viscosities and thus shifting the maximum value of the peak slightly leftwards, nevertheless, keeping the same envelope of values for the right side of the peak as in the 26 km width of the mantle.

The last examined figure for Enceladus is the Fig. 3.6. There is no big difference in the graph in comparison to the case of 26 km width of mantle, nonetheless, in case of Maxwell model, the whole curve has shifted a bit leftward towards the lower viscosities with no change in the maximum value of viscosity and keeping the shape of the curve the same. On the contrary, the Kelvin-Voigt curve shifts only slightly downwards which decreases the overall heating power caused by the tidal forces. The position of the peak has not changed in terms of viscosity and keeps on being approximately 10^{14} Pa s.

Figure 3.4: Enceladus - Radial displacement (52 km width)
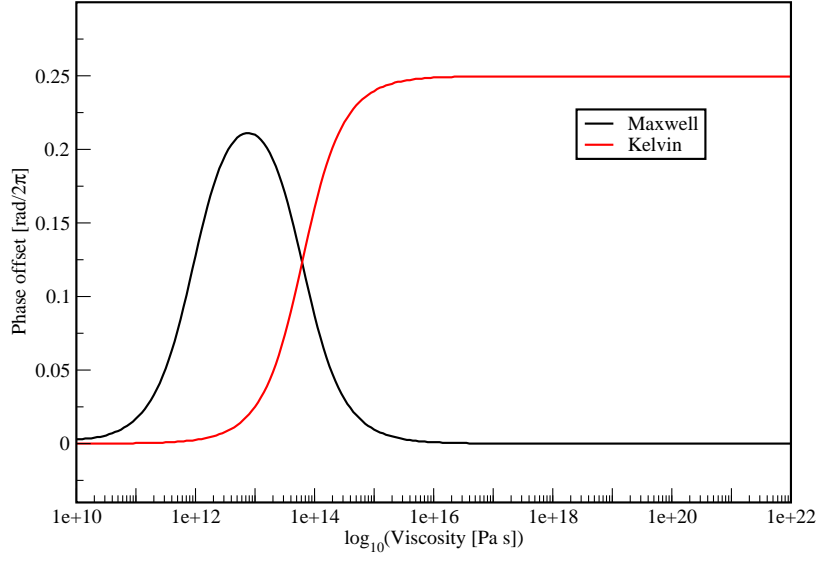
Figure 3.5: Enceladus - Phase offset (52 km width)
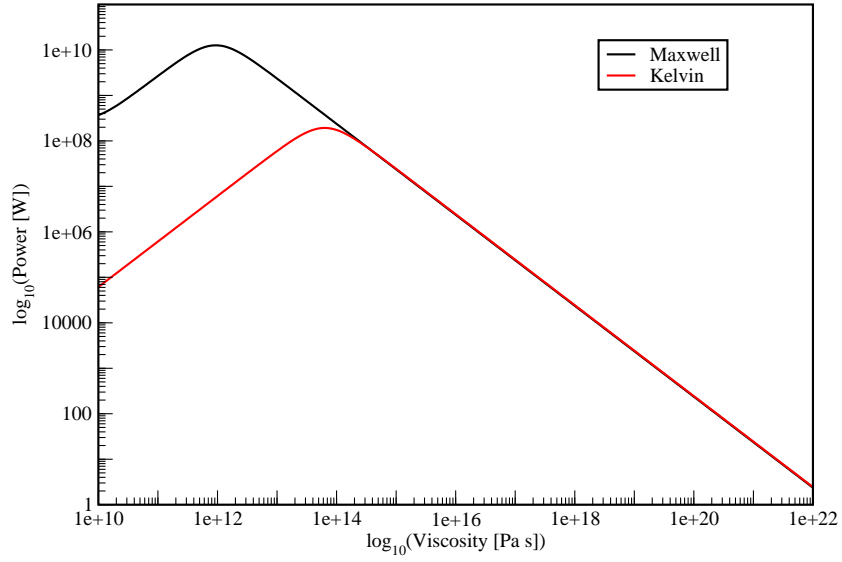
Figure 3.6: Enceladus - Power (52 km width)

3.2.2 Europa

Similarly to Enceladus, Jupiter's moon Europa is also an icy moon. The substantial difference is in the size of the moon. Europa with its 1561 km radius makes it almost 240 larger in terms of volume than Enceladus. All other parameters are quite similar to the Enceladus but slightly adjusted to a larger body (e.g.

gravitational force). Therefore, in the following figures, we are mainly looking for the role of the planetary body size in determination of the computed parameters.

If we compare the Fig. 3.7 to Enceladus, there is an obvious shift of the elastic limit upwards almost to the point where the limit was for the low viscosities in case of Maxwell model. This causes the fact that the amplitude of the radial displacement is in case of Maxwell model almost the same for all studied viscosities, reaching again the elastic limit for higher viscosities. In case of Kelvin-Voigt model, the turning point where the radial displacement starts to decrease shifted more towards higher viscosities between 10^{15} Pa s and 10^{16} Pa s.

The difference in the phase offset depicted by Fig. 3.8 is significant mainly in case of Maxwell model. There is a huge change in the size of the peak which was substantial in case of Enceladus but almost negligible in case of Europa. The remnants of the peak changed its position rightwards to the point where the phase offset predicted by Kelvin-Voigt model starts to grow. This increase has also slightly shifted rightwards as it is growing between the 10^{14} Pa s and 10^{16} Pa s viscosities which is 10 times higher than in case of Enceladus.

The most surprising result is, however, depicted in the Fig. 3.9. The surprise lies in the fact, that in case of Enceladus, the model which predicted higher heating power was Maxwell model whereas now it is Kelvin-Voigt model. There must be made a remark that in this case the viscosities for which the Kelvin-Voigt model is higher are above 10^{14} Pa s whereas in case of Enceladus the power was higher for lower values of viscosity (in case of Maxwell model). Therefore the two cases differ significantly. They also vary in the amount of produced heat, namely, Europa produces around 100 GW of heating power in its maximum at viscosity about 10^{14} Pa s according to Maxwell model. Moreover, according to Kelvin-Voigt model, the heating power is about 2000 GW when the viscosity is between $10^{1}5$ Pa s and $10^{1}6$ Pa s.
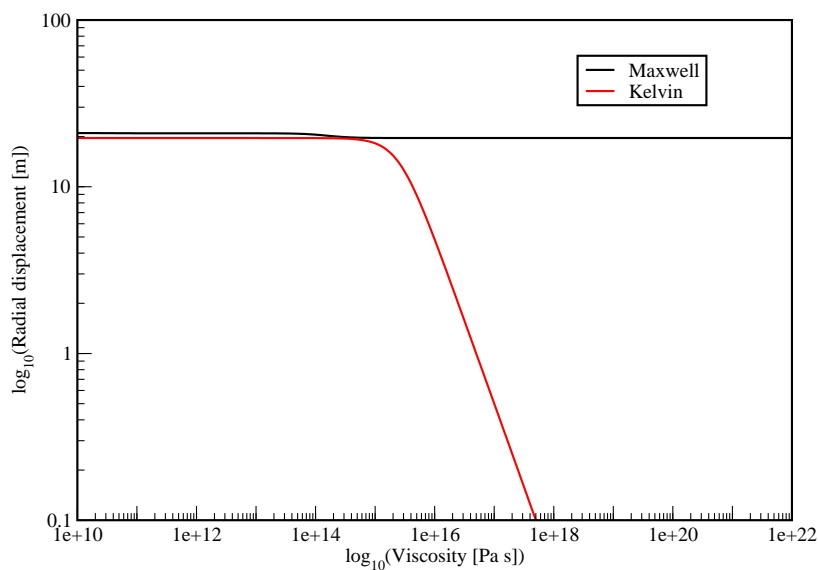
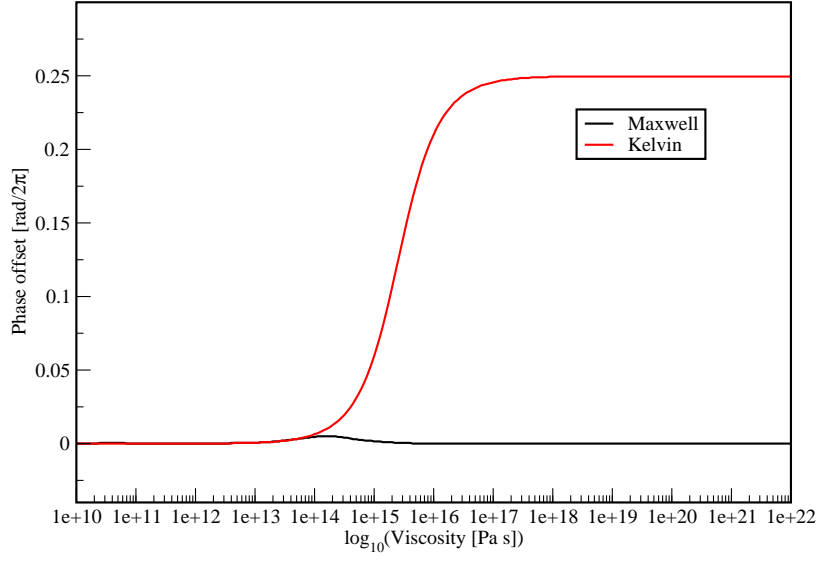

Figure 3.7: Europa - Radial displacement
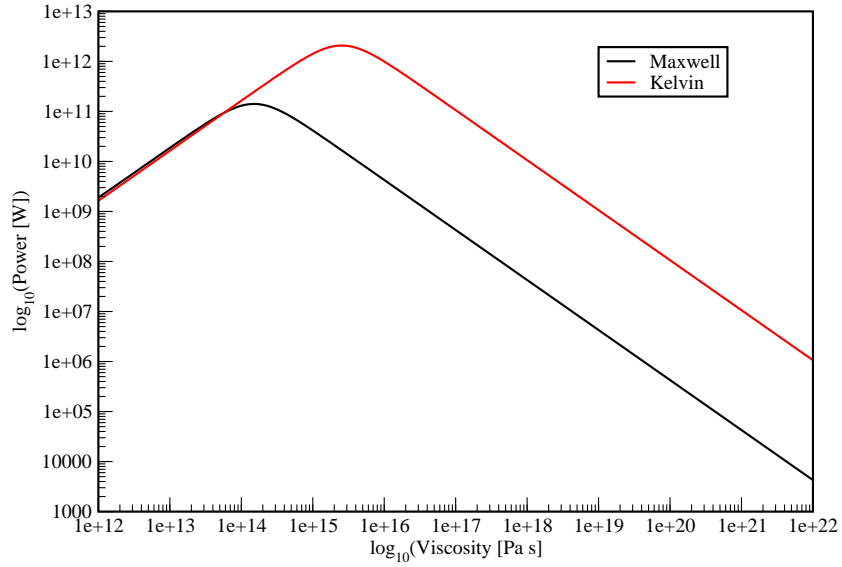
34

Figure 3.8: Europa - Phase offset

Figure 3.9: Europa - Power

3.3 Silicate bodies

As there might be significant differences in predicting the generated heat also in case of larger planetary bodies comprised mainly of silicates as shown by Henning et al. (2009), we study also these. The first silicate planetary body studied is an

imaginary exoplanet with parameters similar to the Earth, which is studied for four different orbital periods. The second is located in the Solar System and it is Mercury which is characteristic by different tidal potential as it is tidally locked with the Sun in a 3:2 resonance. The main difference in comparison to the icy moons is that in case of silicate bodies, there is much higher shear modulus (70 GPa), and also much higher density gradient at the bottom boundary of the mantle.

3.3.1 Exoplanet

The exoplanet is assumed to have an extreme density gradient of $7500\,\text{kg}\,\text{m}^{-3}$ at the interface between the mantle and the core of the planet. Also the relative size of the mantle is assumed much different from the icy moons which makes it in this case exactly one half of its radius. Such a planet was examined for different orbital periods in order to find out its effect on the studied parameters.

From the Fig. 3.10 it is apparent that the radial displacement results do not vary much from the results obtained for the icy moons, especially in terms of shape of the curves. The only difference lies in the scale which decreases with increasing orbital period and obviously there is some kind of linear relationship between the shift of the curves and the orbital period. The viscosities, where a turning point for the Kelvin-Voigt model occurs and the amplitudes start to decrease there dramatically, are higher than in case of icy moons. The values especially depend on the orbital period and lie between $10^{15} Pa \cdot s$ and $10^{17} Pa \cdot s$.

In terms of phase offset as can be seen in Fig. 3.11, there is relatively small peak in case of Maxwell in comparison to Enceladus but relatively large peak if compared to Europa, the shape is however very similar to icy moons with the same limits as previously. An interesting effect of the orbital period can be seen i.e. as it grows the whole curve shifts to the right towards higher viscosities. That means when we increase the orbital period we have to increase also the viscosity in order to keep the phase offset of the radial displacement still the same.

The Figure 3.12 depicts how the shrinking orbital period increases the tidal deformations of the exoplanet reaching over 100 billion of GW if it has one day lasting orbital period. As the orbital period increases the power rapidly decreases and the maximum moves towards higher viscosities for both Maxwell and Kelvin-Voigt models. The interesting observation is a different mutual position of the particular Maxwell and Kelvin-Voigt curves because they do not merge at neither high nor low viscosities and thus opposing the figures depicting power shown for the icy moons. The discrepancy can be seen for all orbital periods, and therefore this property is probably caused by high density gradient and overall massive size.
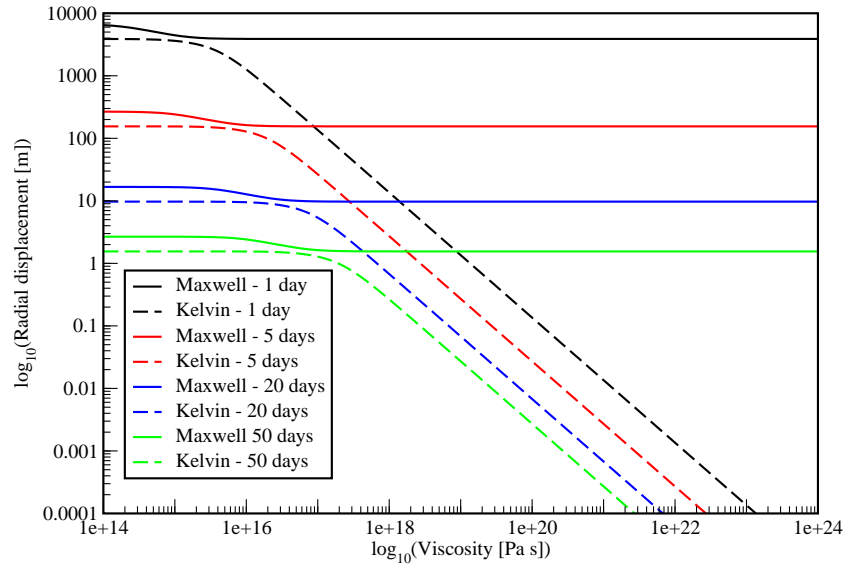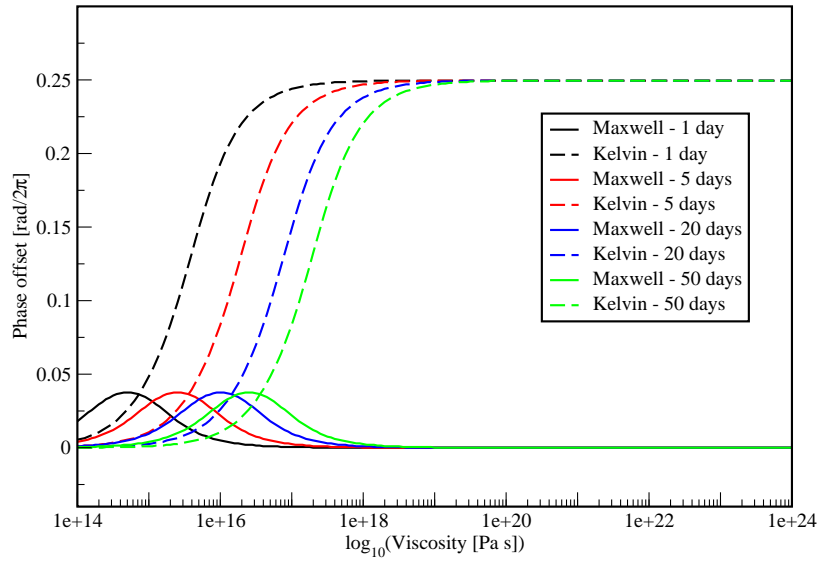
Figure 3.10: Exoplanet - Radial displacement

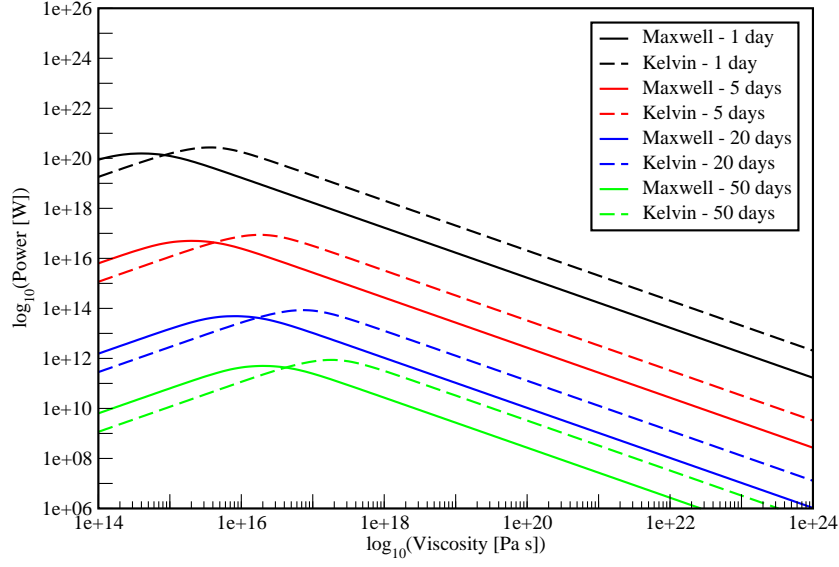Figure 3.11: Exoplanet - Phase offset

37

Figure 3.12: Exoplanet - Power

3.3.2 Mercury

Mercury is the closest planet to the Sun which expose it to an enormous portion of energy and radiation from the Sun. Apart from that, there is one more special property which makes Mercury unique in the Solar System and very interesting for us in comparison of the Maxwell and Kelvin model. The property is, as was stated in the beginning of the silicate bodies section, the 3:2 asynchronous rotation making the years on the Mercury shorter than days. Until this moment we studied only planetary bodies which have synchronous rotation. However, with the introduction of the asynchronous rotation, the tidal forces might have different functional form i.e. something which can have a very significant impact on studied variables and show more interesting differences between the Maxwell and Kelvin model. The tidal forces are given by the tidal potential as stated in chapter 2. The tidal potential for Mercury $\varphi_{Mercury}$ similarly as stated in Balogh & Giampieri (2002) is given by

$$
\begin{aligned}
\varphi_{Mercury} = &- \sqrt{\frac{9\pi}{5}} r^2 \omega^2 e \left(\cos \omega t + \frac{3}{2} e \cos 2\omega t \right) Y_{20} \\
&+ \sqrt{\frac{3\pi}{10}} r^2 \omega^2 \left((1 + 6e^2) \cos \omega t - \frac{1}{2} e \cos 2\omega t \right) (Y_{22} + Y_{2-2}) \\
&+ \sqrt{\frac{3\pi}{10}} r^2 \omega^2 \left((1 - 11e^2) i \sin \omega t - \frac{1}{2} e \, i \sin 2\omega t \right) (Y_{22} + Y_{2-2}).
\end{aligned}
\tag{3.1}
$$

In the Figure 3.13 there are two dramatical changes in comparison to the previous bodies examined. The first change is that a limit for high viscosities in case of Maxwell model and a limit for low viscosities in case of Kelvin-Voigt model are no longer the same. The second change is that there is another unexpected

increase of the amplitude between the relatively low viscosities for Mercury i.e. around 10^{15}Pa s which is probably a consequence of the different tidal potential caused by the asynchronous rotation.

Next, the phase offset characterized by Fig. 3.14 has two peaks instead of the only one which was described at all preceding bodies. The second peak is not so large and can be found only on the Maxwell curve and it is located again around the viscosity 10^{15}Pa s with the similar explanation as in the previous figure. What is also interesting is that Kelvin model, though it looks very similarly as in case of different bodies, has different limit for high viscosities. The phase offset has been measured by the relative offset of the maximum amplitude against the elastic model and has, however, quite unusually skewed towards the elastic part and thus changed the phase offset a bit downwards.

The last figure 3.15 shows us curves which we could be familiar with from the exoplanet results. Relative positions of maxima between the Maxwell and Kelvin-Voigt model are very similar to the ones that have been already examined previously. Also their magnitude is consistent with the fact that Mercury is a silicate body and thus there is a large density gradient between the mantle and core. The magnitude is small in comparison to exoplanets because there is a long orbital period lasting almost 88 days and resulting thus in similar tidal heating as in case of Enceladus. There is however a bit different shape for Maxwell curve than usually. There is an inflection point in power around the viscosities near 10^{15} Pa s, probably again as a a result of changed tidal potential.
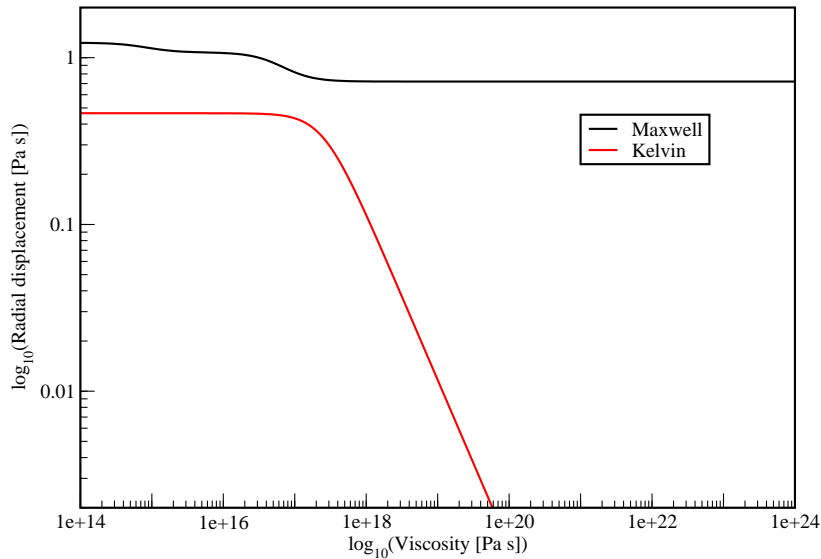

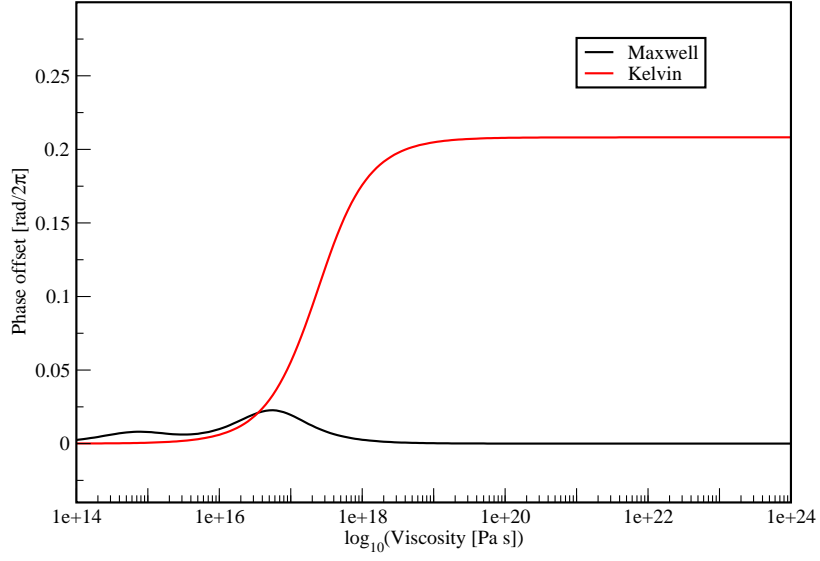Figure 3.13: Mercury - Radial displacement
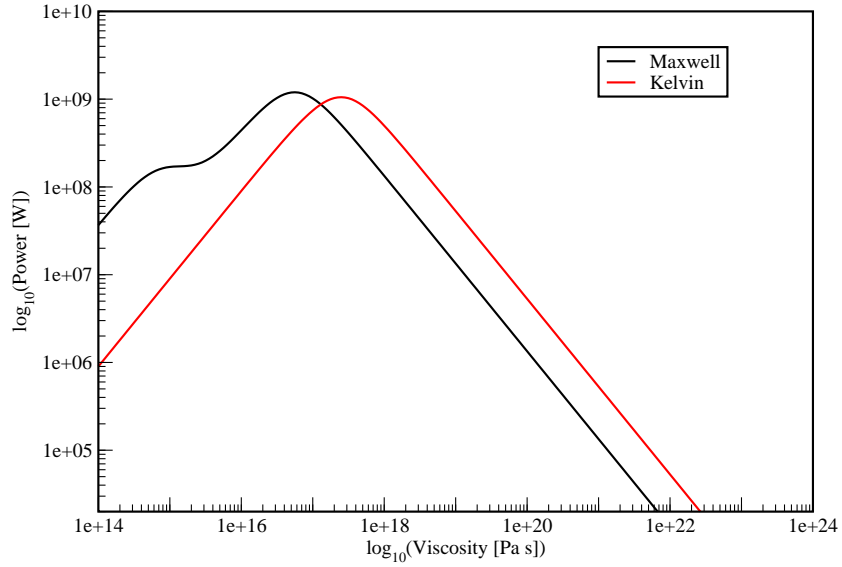
Figure 3.14: Mercury - Phase offset

Figure 3.15: Mercury - Power

3.4 Discussion

A wide variety of planetary bodies was examined in the detail in order to find out which model predicts the generated heat by tidal deformation better. Practically for all the bodies, the Maxwell and Kelvin-Voigt models are very different both

in terms of magnitude and in terms of shape of the curves. In the following discussion we try to suggest some general conclusions about the models and their parameters.

The parameter which we examined especially in case of Enceladus, namely, the width of the mantle seems to not change the magnitude of the dissipated energy caused by the tidal forces in case of Maxwell model whereas in case of Kelvin the dissipated energy decreases with the increasing width of the mantle. This shows that both models control for different effects. Maxwell model is a valid approximation in case of the long term lasting processes and therefore there might exist some effects in the mantle on much more detailed scale which could be better described by the Kelvin-Voigt model in short run.

Maxwell model predicted generally higher power for Enceladus whereas Kelvin-Voigt model predicted it vice versa for Europa. Our suggestion is that the power predicted by Kelvin-Voigt model might be not only a result of greater size of the body, but also a far smaller relative size of the mantle in comparison with the rest of the body and thus behaving like a thin mantle around the huge core. The relative difference between the dissipated energy were shown also in case of silicate bodies, where the magnitudes were similar for both models probably because of high density gradient between the mantle and the core, however, Kelvin-Voigt predicted them generally for higher values of viscosities.

The strong dependence has been shown in case of the orbital period which is crucial in determination of the magnitude of the dissipated energy. The shorter the period is, the more power it produces as the body is subject to much more frequent deformations and thus it has less time to stabilize its shape. Due to this fact, we suggest Kelvin-Voigt model might suit quite well for lower orbital periods as there might exist some processes which are in their nature reversible.

Asynchronous rotation such as has Mercury, has shown the different rotation can change the shape of all studied function in case of Maxwell model. Interestingly, the shapes of the curves for Kelvin-Voigt model are very similar to the all previously examined and thus it seems like the Kelvin-Voigt model can ignore different timespans of Mercury's own rotation and revolution about the sun. The possible suggestion is the model behaves as if the rotation was so slow, that it does not matter that the rotation is asynchronous.

However, all the suggestions we might have been firstly tested on larger varieties of bodies which might be seen as an possible extension of this work. Far more important is, however, the question, whether are we able to understand different results the Kelvin-Voigt model offers. The viscosity as a parameter can be interpreted differently in such a model than the well known viscosity used in the Maxwell model. If we have a viscosity parameter for which the body is completely solid if the viscosity is zero as in Kelvin-Voigt model, can we still use the same viscosity and intuition for the materials we know?

There is a good chance the additional deformation model could explain some effects, however it is important to better establish the intuition behind them which might be the hardest part. From the models studied there it is obvious there is not an easy e.g. reciprocal relationship between the two different viscosities as someone might perhaps suggest. The relationship is more complicated and it could help to try also more complicated models known from the mechanical engineering in order to find out the true pros and cons of the models which could

be also an extension of this work.

It is important to remark our model is a very simplified 3D model which assumes the list of the following: The planetary bodies are perfect balls, there is no lateral stirring, no temperature dependence, no changes in shear modulus as the depth changes, and there is no dependence of the parameters stated in the table 3.1 on the time, depth or anything else which might be important in their determination. Furthermore, One of the hugest simplifications is an assumption of global ocean under the mantle and also the restricted number of layers in the mantle due to discretization. Last but not least, the computation might have been more precise if we used also higher spectra with $j > 2$ which were not calculated in this thesis.

Conclusion

This thesis has introduced the topic of whether the Kelvin-Voigt anelastic model can be used in some situations to describe the dissipation of planetary bodies. The dominantly used Maxwell model is, namely, only one out of many possibilities which can be used. On the other hand, other models do not have as clear interpretation as the Maxwell model offers, and therefore it may be enticing to use it.

In the thesis, the goal was to find the main differences between these two models. In order to do so, a 3D mathematical model has been derived characterizing quite comprehensively a planetary body with the shape of a ball. A substantial part of the work is devoted to different points of view on the anelastic deformation and thus the thesis introduced Maxwell and Kelvin-Voigt models, which were implemented in the 3D model. Consequently a computer simulations were made by independently developed Fortran program in order to compare the differences predicted by the two models which was the aim of this thesis.

The models were applied to various planetary bodies, especially the icy moons Enceladus and Europa where the alternative deformation models such as Kelvin-Voigt could better explain the dissipative processes. Further extensions of the application were done in case of Earth-like exoplanet and Mercury where an asynchronous rotation occurs creating thus new space for differences of the two models.

We showed that the models differ significantly for all planetary bodies examined and that both models predict another rate of dissipation in different situations with no exact reason found why one model should describe the reality better than another. The specific results were discussed throughout the results chapter.

Future extensions of this work might add more deformation models or more planetary bodies in order to compare better the properties of the particular models used. A lot of simplifications has been made, which were discussed especially in the discussion section, and thus there is still a lot of improvements which could extend the thesis in the future.

Bibliography

Balogh, A. & Giampieri, G. (2002), 'Mercury: the planet and its orbit', *Rep. Prog. Phys.* **65**, 529–560.

Chen, E. M. A., Nimmo, F. & Glatzmaier, G. (2014), 'Tidal heating in icy satellite oceans', *Icarus* **229**, 11–30.

Golle, O., Dumoulin, C., Choblet, G. & Čadek, O. (2012), 'Topography and geoid induced by a convecting mantle beneath an elastic lithosphere', *Geophys. J. Inter.* **1**, 55–72.

Henning, W., O'Connell, R. J. & Sasselov, D. D. (2009), 'Tidally heated terrestrial exoplanets: Viscoelastic response models.', *Astrophys. J.* **707**, 1000–1015.

Kaula, W. M. (1964), 'Tidal dissipation by solid friction and the resulting orbital evolution', *Rev. Geophys.* **2**, 661–685.

Matas, J. (1995), Mantle viscosity and density structure, Master's thesis, Faculty of Mathematics and Physics, Charles University.

Moore, W. & Schubert, G. (2000), 'The tidal response of europa', *Icarus* **147**, 317–319.

Peltier, W., Drummond, R. A. & Tushingham, A. M. (1986), 'Post-glacial rebound and transient lower mantle rheology', *Geophys. J. R. astr. Soc.* **87**, 79–116.

Prockter, L. M. & Pappalardo, R. T. (2007), *Encyclopedia of the Solar System*, second edn, Elsevier.

Ross, M. N. & Schubert, G. (1989), 'Viscoelastic models of tidal heating on enceladus', *Icarus* **78**, 90–101.

Roylance, D. (2001), 'Engineering viscoelasticity'.
URL: *http://web.mit.edu/course/3/3.11/www/modules/visco.pdf*

Tobie, G., Čadek, O. & Sotina, C. (2008), 'Solid tidal friction above a liquid water reservoir as the origin of the south pole hotspot on enceladus', *Icarus* **196**, 642–652.

Tyler, R. H. (2009), 'Ocean tides heat enceladus', *Geophys. Res. Lett.* **36**(L15205).

Zhong, S. & Zuber, M. T. (2000), 'Long-wavelength topographic relaxation for self-gravitating planets and implications for the time-dependent compensation of surface topography', *J. geophys. Res.* **105**, 4153–4164.

List of Figures

List of Tables

Attachments

Attachment 1: CD containing the developed program in Fortran.